UNIVERSIDADE DE LISBOA

FACULDADE DE CIÊNCIAS

DEPARTAMENTO DE FÍSICA

Study of the Effect of Magnetic Field on PET/MR Systems: GATE Monte Carlo Simulations

André Rodrigues Diogo

Mestrado Integrado em Engenharia Biomédica e Biofísica

Perfil em Radiações em Diagnóstico e Terapia

Dissertação orientada por:

Prof. Dr. Stefaan Vandenberghe

Prof. Dr. Nuno Matela

2019

Acknowledgements

I would like to start by thanking Prof. Stefaan Vandenberghe for giving me the opportunity to be a part of this amazing project and welcoming into the Medical Imaging and Signal Processing research group from Ghent University. I also want to thank the Erasmus+ Program for the opportunity and funding I got for this internship. Thank you to Prof. Nuno Matela for the counselling and having encouraged me to choose Ghent as the place for my thesis.

I want to express all my gratitude towards my mentor throughout this journey, Paulo Caribé. Thank you for always being there to answer my questions, for all the support and guidance and encouraging words, for always believing in me, and, most important, for the friendship.

Thank you also to everyone at Medisip for being so welcoming and nice, since day one. The year would not have been the same without all of you!

Thank you to Marta, Catarina and Tomás, my best buddies, who were always ready to hear me complain about anything and have supported me continuously throughout the last few months, even when we were thousands of kilometers apart.

Thank you to my parents and my sister for always being there, for always encouraging and pushing me, motivating me through these months away from everyone and everything I knew. Nothing would have been possible without your support. To my aunt, grandma and grandparents and all the family who provided me with enough chocolate to give diabetes to at least 50 children.

Abstract

The latest developments in PET technology have allowed for its integration with MR scanners as a superior alternative to PET/CT imaging, especially useful in instances such as detection of low-grade tumours and prostate cancer resurgence. However, the magnetic field inherent to the MR introduces some challenges and uncertainty regarding the scanners' performance. Furthermore, novel radiopharmaceuticals that feature a wide range of radioisotopes with different properties have been introduced in the market and are being used more and more in clinical contexts. Thus, it is relevant to study how PET/MR systems perform when using such radioisotopes, and the impact the magnetic field has on the performance, as a way to better understand these scanners and optimize clinical practices. Recently, total-body PET scanners that entirely cover the patients, or large portions of the body, have also been introduced.

In this dissertation, NEMA sensitivity and count rate statistics tests are performed on a realistic model of the GE Signa PET/MR scanner through GATE Monte Carlo simulations, using the prescribed ^{18}F, as well as using other radioisotopes such as ^{11}C, ^{13}N, ^{15}O, ^{68}Ga and ^{82}Rb, which feature positron energies from 633 keV do 3.3 MeV. The same studies are performed on a conceptual 1.04 m long PET scanner to study the potential performance of such a scanner. Also, a study of the positron range of the same radioisotopes in tissues of varying density was done in order to estimate the impact of the magnetic field. On the GE Signa PET/MR, the sensitivity test results are in line with published values and show a clear dependence on the positron branching ratio, with the pure β^+ emitters having the highest sensitivity values, 21.50 cps/kBq for ^{13}N in the presence of a 3 T MR field. The magnetic field increases sensitivity up to 5% for the higher energy radioisotopes, due to constraints on positron range preventing positron from escaping the phantom tube. The move to TB-PET shows a tremendous increase of up to 7 times the sensitivity, peaking at 177.87 cps/kBq for ^{13}N. Regarding the NECR test, the simulation results on the GE Signa PET/MR are confirmed by the published values regarding ^{18}F, with the other pure β^+ emitters showing comparable peak NECR values. However, ^{68}Ga and ^{82}Rb have much lower peak NECR values, due to the 3.0% and 14.2% additional prompt-gamma emission, which contaminate the acquisition and contribute to detector busyness, effectively lowering NECR.

Studies on positron range show strong dependence on the tissue density. The 3 T magnetic field introduces significant constraints on positron range in the transversal plane which can mean up to 4 times smaller range in the x and y directions when compared with the z direction, the direction of the MR field, which shows differences only in terms of density distribution but not absolute values.

The results obtained in this dissertation point out the need to re-evaluate the different image reconstruction algorithms for PET/MR imaging, given the discrepancies between the transversal and axial ranges under a magnetic field, as well as the adaptation of the NEMA performance measurements protocols for scanners with long axial fields of view, and, to some extent, to be performed with different radioisotopes. However, there are some limitations to the conclusions drawn from the work presented, such as the fact that the method used to estimate NECR and the related measures can underestimate them due to uncertainty regarding dead time set-up.

The work developed in this thesis and the achieved outcomes have real world applications in more than one area. Learning how scanners perform under difference circumstances, i.e. using different

radioisotopes, can help clinics better prepare their schedules according to predicted scanning times, optimize activity quantities injected into patients, and overall improve the patient throughput. Furthermore, possible applications in reconstruction algorithms that may improve the quality of the produced imaged and help to diagnose and/or better identify multiple diseases, leading to general improvements in public health through screening programs and early diagnosis.

Resumo

Tomografia por emissão de positrões (PET, na sigla em inglês) é uma técnica de imagem de medicina nuclear que tem por base a emissão de positrões e a sua consequente aniquilação com as suas anti-partículas, electrões. Ao acoplar radioisótopos emissores de positrões a moléculas orgânicas, é possível seguir e quantificar diversos processos metabólicos que ocorrem no corpo, fazendo da PET uma técnica de imagem funcional. Sendo uma técnica de imagem funcional, com informação anatómica quase inexistente, a PET é frequentemente aliada a outras técnicas que ofereçam essa informação. Desde o aparecimento de scanners integrados PET/CT no início do século, estes sistemas tornaram-se extremamente populares. No entanto, sistemas integrados PET/MR surgiram no mercado nos últimos anos e têm vindo a ganhar popularidade devido às suas vantagens sobre PET/CT, tais como um contraste entre tecidos moles bastante superior e a eliminação da dose de radiação inerente à CT.

A presença do campo magnético proveniente da MR introduz alguns desafios na porção PET dos sistemas integrados, nomeadamente no impacto do campo no comportamento dos radioisótopos, alterando a trajetória dos positrões emitidos para uma trajetória em hélice como resultado da força de Lorentz. Além disso, os testes NEMA de caracterização do desempenho de scanners PET/MR são apenas realizados com ^{18}F. Dados os avanços em radiofarmacêutica, torna-se relevante e importante o estudo do desempenho destes scanners quando utilizados diferentes radioisótopos, nomeadamente a realização de testes NEMA.

Com o objetivo de estudar e quantificar tanto o efeito do campo magnético no alcance dos positrões e na performance de scanners integrados PET/MR, como as diferenças na utilização de diferentes radioisótopos, foi construído um modelo realista do scanner GE Signa no qual podem ser realizadas simulações Monte Carlo dos testes NEMA de sensibilidade e NECR usando o toolkit GATE. Foram ainda desenvolvidos os scripts analíticos em Python, ROOT e MATLAB para análise dos resultados dos diferentes testes. A validação das simulações foi feita através da comparação com valores publicados, medidos experimentalmente num scanner GE Signa. Os mesmos testes foram aplicados a um sistema PET de corpo inteiro, com extensão axial de 104 cm, de modo a estudar o potencial desempenho de um sistema com estas características. Além disso, foi ainda estudado o efeito do campo magnético no alcance dos positrões em diferentes tecidos.

O teste de sensibilidade mede a capacidade de um scanner em registar coincidências, sendo medida em contagens por segundo para um determinado nível de atividade (cps/kBq). A simulação deste teste requer a construção do seu respetivo fantoma, que envolve 5 camadas cilíndricas de alumínio com espessura constante, bem como a análise de dados prescrita pela NEMA. Para as simulações realizadas no GE Signa PET/MR sem campo magnético, no caso dos emissores β^+ puros ^{11}C, ^{13}N e ^{15}O, os resultados obtidos foram de 20.53, 20.65 e 20.31 cps/kBq, respetivamente, sendo comparáveis com o de ^{18}F, 20.75 cps/kBq. ^{68}Ga oferece também resultados semelhantes aos teóricos, 18.10 cps/kBq. Todos estes resultados estão de acordo com o esperado, dado que a fração de emissão de positrões é o fator mais significativo da sensibilidade. Quanto ao ^{82}Rb, os valores obtidos são significativamente mais baixos que os previstos. Esta diferença pode ser explicada pela alta energia e longo alcance dos positrões provenientes deste decaimento, que têm alta probabilidade de não perderem a sua energia na primeira camada de alumínio, influenciando negativamente a análise de resultados, subestimando o valor real de sensibilidade. Aquando da aplicação do campo magnético de 3 T, as diferenças registadas em relação

aos valores medidos e publicados são mínimas, e os valores simulados são até 5% maiores do que sem a presença do campo magnético, sendo que esta diferença aumenta à medida que aumenta a energia dos positrões. As mesmas conclusões são retiradas das simulações realizadas com o TB-PET. No entanto, os valores neste são significativamente mais elevados, sendo entre 5 a 7 vezes maiores do que os resultados obtidos no GE Signa, chegando a um máximo de 174.27 cps/kBq, já que, no TB-PET, a fonte é completamente coberta pelo scanner enquanto que apenas certa de 1/3 da fonte é coberta pelo GE Signa, deixando grande parte da atividade fora do scanner.

O teste de NECR e estatísticas de contagem tem o objetivo de medir fontes altamente energéticas e reconhecer radiação dispersa, tal como radiação gama adicional. NECR é uma medida que está localmente relacionada com SNR, com a dose de atividade que é necessário administrar aos pacientes para obter imagens, e ainda com a duração dos exames. Usando o fantoma de dispersão (*scatter phantom*), e analisando os dados através de sinogramas, é possível obter três taxas de contagem: coincidências verdadeiras, dispersas e aleatórias, através das quais se calcula o valor do pico de NECR e o nível de atividade a que este ocorre. No GE Signa PET/MR, em a presença do campo magnético, os isótopos ^{11}C, ^{13}N e ^{15}O demonstram resultados de pico de NECR de 206.77, 201.72 e 196.08 kcps, próximos do valor obtido para ^{18}F, 209.32 kcps, como seria de esperar tendo em conta as semelhanças das propriedades de decaimento. No ^{68}Ga e ^{82}Rb, estes valores são significativamente mais baixos, 185.70 e 136.93 kcps, respetivamente, sendo notável a clara influência dos fotões gama imediatos nos dois isótopos, com maior expressão no ^{82}Rb. O registo destes fotões contribui significativamente não só para o aumento do número de coincidências aleatórias registadas, como também para os efeitos do tempo morto do detetor, que leva a uma deterioração da capacidade do detetor de registar os fotões provenientes da aniquilação dos positrões e, consequentemente, registo de coincidências verdadeiras. Os resultados do mesmo teste aplicando um campo de magnético de 3 T, o pico de NECR para todos os isótopos teve um aumento até 8%, mais significativo para os isótopos que emitem positrões com mais alta energia, sendo que no caso do ^{82}Rb, este pico chegou aos 173.50 kcps. Relativamente ao TB-PET, os aumentos de pico de NECR registaram-se na ordem das 7 a 8 vezes maiores que os valores obtidos no GE Signa. Neste scanner com 104 cm de comprimento, o pico de NECR chega aos 1624.54 kcps aquando da aplicação do campo magnético, efetuando o teste com ^{18}F. Ainda seguindo a tendência registada anteriormente, ^{68}Ga e ^{82}Rb apresentam resultados muito inferiores aos emissores β$^+$ puros. Neste scanner, é notável ainda uma maior discrepância entre os diferentes isótopos.

O facto de as diferenças entre a aplicação ou não do campo magnético serem da mesma magnitude nos dois scanners pode sugerir que os efeitos são específicos aos protocolos NEMA e ao teste aplicado, e não se traduzem necessariamente para o contexto clínico e aquisições com pacientes. No entanto, estabelece-se uma relação com os constrangimentos impostos ao alcance dos positrões em ambos os testes. Por um lado, os constrangimentos ao alcance dos positrões no plano transversal à direção do campo magnético são notáveis pelo aumento do número de coincidências registadas nos primeiros cilindros de atenuação de alumínio, efetivamente aumentando o valor final calculado para a sensibilidade, particularmente para isótopos de alta energia. Por outro, os mesmos constrangimentos causam um aumento do número de coincidências detetadas próximas da fonte de radioatividade, o que, no processo de análise de dados, contribui significativamente para o aumento do número de coincidências verdadeiras e, consequentemente, NECR.

O estudo do alcance dos positrões dos diferentes isótopos revela uma redução significativa do alcance tridimensional aquando da aplicação do campo magnético. Esta redução é sentida apenas no plano transversal (direções *x* e *y*), sendo que o alcance axial (direção *z*) se mantém em termos de valores absolutos. A distribuição de densidade dos pontos de aniquilação, ou do alcance axial, no entanto, apresenta-se alongada, devido aos constrangimentos no plano transversal. Além disso, é ainda notável uma forte dependência destes efeitos tanto na energia dos positrões como na densidade do tecido, sendo

que o alcance transversal pode ser até 4 vezes menor que o axial para altas energias, em tecidos pouco densos.

Assim, conclui-se que o uso de diferentes isótopos tem um impacto significativo na performance de sistemas integrados PET/MR, com o campo magnético inerente à RM introduzindo diferenças no comportamento dos isótopos, especificamente constrangimentos no alcance dos positrões no plano transversal. Além de otimização de planos de aquisição de imagens em contexto clínico, os resultados obtidos nesta dissertação podem ser futuramente aplicados em software de reconstrução de imagem, tendo em conta as limitações referidas.

Palavras-chave: PET/MR; GE Signa; testes NEMA; sensibilidade; NECR; alcance dos positrões; simulações Monte Carlo; GATE

Table of Contents

List of Figures

List of Tables

List of Abbreviations

AFOV	Axial Field of View
cps	Counts per second
CT	Computed Tomography
FBP	Filtered Back Projection
FOV	Field of View
FWHM	Full Width at Half Maximum
FWTM	Full Width at Tenth Maximum
GATE	Geant4 Application for Tomographic Emission
keV	Kilo-electronvolt
LOR	Line of Response
LYSO	Lutetium Yttrium Orthosilicate
MeV	Mega-electronvolt
MRI	Magnetic Resonance Imaging
NECR	Noise Equivalent Count Rate
PET	Positron Emission Tomography
PMT	Photomultiplier Tube
SNR	Signal-to-noise Ration
SPECT	Single-photon Emission Computed Tomography
TOF	Time of Flight
TB-PET	Total-body Positron Emission Tomograph

1 Introduction

Over the last century, scientific research has paved the way to the invention and application in medicine of Positron Emission Tomography (PET). Since Dirac's prediction of the positron back in 1929, [1] developments in quantum physics, electronics and biochemistry [2] led the group of Michael Phelps and Michel Ter-Pogossian to build the first prototype of a PET system, called Positron Emission Transaxial Tomograph (PETT), [3] based on Kuhl and Edwards' concept of image reconstruction of source distributions. [4] With the introduction of radiopharmaceuticals in the 1970s, particularly the development of ^{18}F-fluorodeoxyglucose (FDG), [5], [6] the technology claimed the attention of the medical community, which allowed for the study of specific metabolic pathways, making PET a functional imaging technique using widely in clinical routine.

Since those days, PET systems have seen an incremental upgrade in their performance and designs, as well as the development of better, more sophisticated models of image reconstruction, among other improvements. Radiopharmaceuticals have also been intensively studied, there being dozens of commercially available variations nowadays. Although it has many applications, this technology is mainly used in cancer diagnosis and staging, as the abnormal cellular growth and intense metabolic needs lead to high uptakes of glucose – which is easily labeled with radioisotopes.

In the last two decades, efforts in advancing the PET technology further have been focused on combining this functional technique with other anatomical techniques, such as computed tomography (CT) and magnetic resonance imaging (MRI). PET/CT was introduced in the late 1990s and has since become extremely popular amongst the medical community. [7] There are many advantages to combining PET scanners with MRI instead of CT. For instance, MRI offers a superior soft tissue contrast when compared to CT, as well a broader range of sequences specific to different body structures, which can have a big impact on diagnosis. Furthermore, radiation dose received by the patient is significantly reduced due to the elimination of the CT, and there is an improvement of PET image quality (resolution, contrast) in the transaxial direction when the exam is performed under strong static magnetic fields, due to the constraint to the positron range. [8] Since the proposal of this effect, in 1986, several studies have been carried out in order to find out how the magnetic field impacts positron range on multiple radiotracers, both experiments and computer simulations. [9]–[16] Despite the advantages, there were many challenges to the integration of MRI with PET systems, such as the PET detector technology, and PET/CT remains the standard for clinical practice, while PET/MR is more commonly used for research. Also, unlike the CT, the MR doesn't provide attenuation coefficients that are fundamental for radiotherapy planning.

Recently, the development of PET scanners took a new turn with the appearance the EXPLORER PET, a PET scanner with an axial field of view (AFOV) of 2 meters. [17], [18] This state-of-the-art scanner comes as a solution to the vast amounts of information left out of conventional scanners, which have AFOVs of only 20 to 25cm.

Through Monte Carlo simulations, this dissertation aims to study how the magnetic field inherent to MRI impacts positron range of a wide variety of commercially available radioisotopes, the changes in performance of the PET portion of hybrid PET/MR scanners, and, finally, study and estimate performance of a conceptual total-body PET/MR system, based on the total-body PET system currently

being developed at MEDISIP research group, which aims to be the European version of the EXPLORER.

In Chapter 2 of this dissertation, an overview of PET and MR imaging principles are presented, divided into three sections. The advantages, disadvantages and challenges of PET/MR imaging and fully integrated systems are also discussed. In Chapter 3, the NEMA protocols for evaluation of PET/MR systems' performance are described. Chapter 4 comprises an introduction of Monte Carlo simulations and GATE, the software used in this dissertation to perform all the simulations needed. In Chapter 5, the methods for building scanner geometries, test set-up and data analysis are described. In Chapter 6, the results obtained from all the simulations are presented, and in Chapter 7 they are analyzed and discussed, and limitations of the work are mentioned. In Chapter 8, the overall conclusions of this dissertation are presented, and future work is discussed. Finally, in Chapter 9, the outcomes from this work are listed.

2 Biomedical Imaging Systems

This chapter comprises an introduction to the imaging systems relevant to this dissertation, positron emission tomography (PET) and magnetic resonance imaging (MRI). Regarding PET imaging, several aspects, such as basic physics, commonly used radioisotopes and instrumentation, will be discussed. On MR imaging, the basic physics will be discussed. Finally, the challenges, advantages and disadvantages of the integration of both modalities on integrated PET/MR systems are described.

2.1 Positron Emission Tomography (PET)

PET is a nuclear imaging technique extremely useful in the measurement and imaging of metabolic activity inside the body. It requires radiotracers containing positron-emitting radioisotopes, such as the ones mentioned below, in Section 2.1.2. Although it can be used multiple fields, such as cardiology and neurology, clinically, this technique is mainly used in oncology, for cancer diagnosis, therapy follow-up, and staging. It has proven a very useful technique in pharmacokinectics to trace biodistribution of new drugs in pre-clinical stages.

2.1.1 Principles of PET Imaging

As the name of the technique suggests, PET relies on the emission of positrons by radioisotopes. Positron emission (β^+ decay) is a type of radioactive decay that occurs when there is a destabilizing surplus of positive charge and energy in the nucleus. In order to become more stable, a proton is converted into a neutron, while simultaneously releasing a positron and a neutrino Equation (2.1). [19]

$$p \rightarrow n + e^+ + \nu \qquad (2.1)$$

After the positron is emitted, it will interact with the matter around it, more specifically with the electrons present in it. When a positron collides with an electron, they will annihilate each other, emitting a pair of gamma photons of 511 keV energy each ($m_e c^2$ = 511 keV), travelling in opposite directions (180 degrees) until they reach the detector crystals (Figure **2.1**). As electrons are abundant in tissues, PET imaging relies on the assurance that the annihilation will take place within a few millimeters from the emission site, allowing for the localization of lesions or process under study. This is dependent on the energy of the positron, which varies from radioisotope to radioisotope.
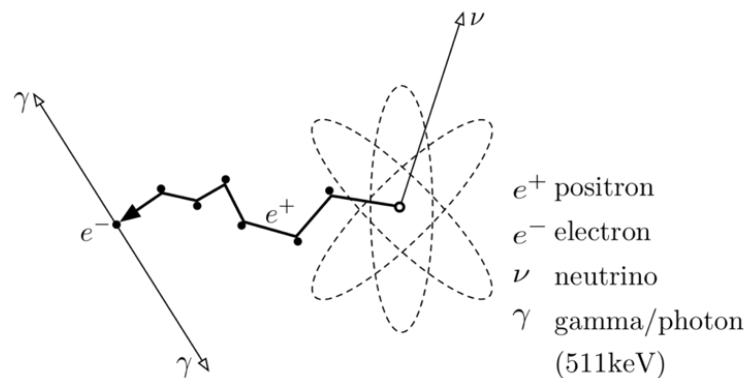
Figure 2.1: Positron-electron annihilation with subsequent emission of 511 keV photons. The positron (e^+) travels some distance before interacting with an electron and being annihilated. [20]

When two photons are caught in the detectors within a certain time window, they are associated with each other and form a coincidence. Each coincidence has its own line of response (LOR), a straight line that connects the two detector blocks, along which the coincidence will have taken place. Although a good approximation in most cases, the localization of the exact site of emission is affected by the emission angle of the photons. The 180º degree mentioned before is an ideal case. In reality, when the linear momentum of both the positron and the electron are not null, there is a slight change in this emission angle (non-collinearity), which will then lead to an incorrectly placed LOR and a misplacement of the annihilation. In addition to non-collinearity, the photons often suffer scattering due to the interaction with the surrounding tissues, completely changing direction. In practical terms, it is not possible to distinguish between coincidences coming from scattered photons of from non-collinear annihilations and in the scope of this work are simply referred to as scattered coincidences. Furthermore, detectors may register hits from simultaneous annihilations from different emissions, or even be absorbed by them via photoelectric effect (discussed below), which will lead to the detection of random coincidences. The different types of detected PET coincidences are represented in Figure **2.2**.
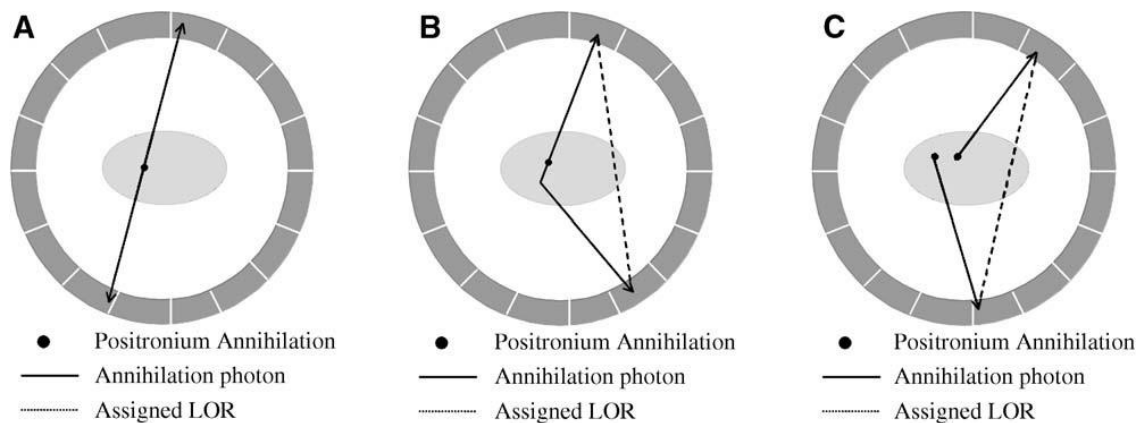
Figure 2.2: Types of coincidences detected in PET imaging. (A) True coincidences. (B) Scattered coincidence. (C) Random coincidence. [21]

Each LOR is defined by two properties: the angle between itself and the horizon, and the perpendicular distance to the center of the scanner, referred to as displacement. When plotting each LOR's two characteristics in a two-dimensional plane, each coincidence is simply a point. The visual representation of every coincidence (thus, every LOR) is a sinogram – the most traditional way of data representation in tomographic imaging. Typically, sinograms take the shape of vertical sine functions, as shown in Figure **2.3**.
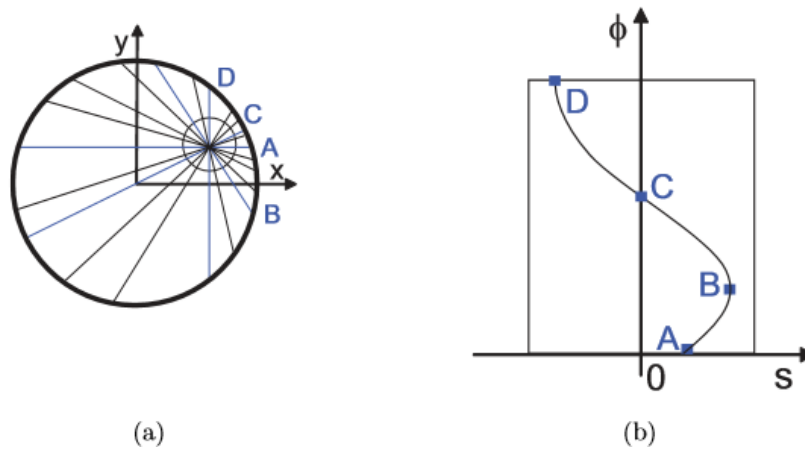
Figure 2.3: Representation of the formation of tomographic imaging sinogram. (A) The position of the source in the scanner. (B) Sinogram of the source, where displacement can be easily understood by the selected LORs and their respective points in the sinogram, represented in blue. [22]

In the case of PET systems, instead of calculating the displacement and angle to the horizon of each LOR, a simpler approach is illustrated in Figure **2.4**. As each LOR is associated with 2 detector blocks, striking a line diagonally across the plane for each of the detectors, will yield an intersection that corresponds to the point in the angle-displacement plane representing the coincidence.
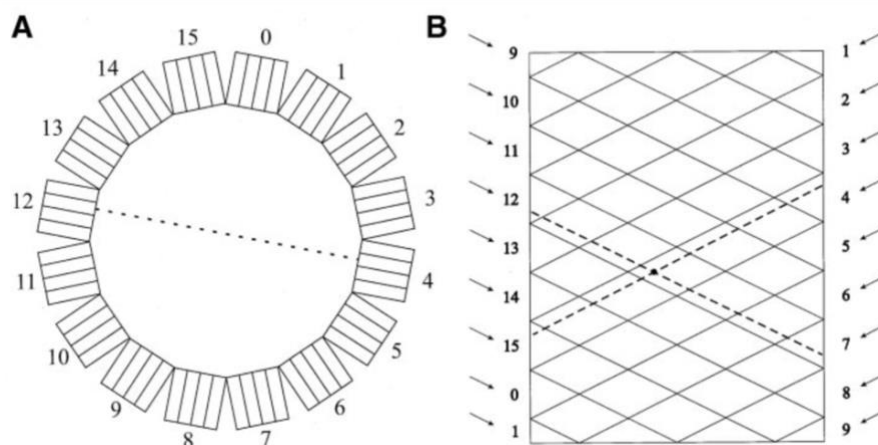
Figure 2.4: Sinogram in PET acquisitions. (A) Profile of the scanner with 16 detector modules and a LOR. (B) Representation of the LOR in the angle-displacement plane.

The data contained in sinograms is used to reconstruct PET images. Multiple image reconstruction algorithms have been developed and were categorized as either analytical or iterative. Analytical algorithms are faster, linear and deterministic. Filtered back-projection (FBP) is the most commonly used analytical method of PET image reconstruction. It is of quite simple and straightforward implementation. The main drawbacks come from the assumption that data is noise-free and don't take into account other degrading factors, such as positron range and noncollinearity. [23]

Iterative methods are more complex methods that rely on statistical estimations of noise and physical effects to estimate images. They are more complex and require more computational power than analytical methods. Instead of a direct solution, the reconstruction improves with each iteration, following certain criteria, until a desired image is reached. Several iterative methods have been developed. The most noteworthy are Maximum Likelihood Expectation Maximization (ML-EM), and its Ordered Subsets Expectation Maximization (OSEM). Main drawback of MLEM is its slow

convergence, while for OSEM is the fact that convergence to the ML solution is not guaranteed. In both cases, the noise is increased with each iteration and requires the images to be smoothed afterwards. [24] No image reconstruction was performed in the scope of this project and the details of the algorithms will not be discussed.

2.1.2 Radioisotopes

PET imaging is based on the annihilation of positron emitted by radionuclides. Although there are hundreds of radionuclides, only a select few of them are positron emitters, with varying properties such as energy or decay mode. Most positron emitter radioisotopes are cyclotron-produced. Before being suitable for the use in medicine, radioisotopes must be attached to an organic molecule or compound to form a radiopharmaceutical, or radiotracer, so that the radioisotopes can be carried to the target place of the examination, through metabolism of the organic molecule. The study of radiotracers is out of the scope of this study, which focus solely on radioisotopes.

The most commonly used radioisotope in PET imaging is fluorine-18 (^{18}F), which has been discovered and intensely studied over half a century ago. [25], [26] Its properties such as half-life, decay scheme and decay energy make it an extremely useful radioisotope for PET imaging, having applications in oncology, neurology, cardiology, and in imaging of organs and structures such as liver or bones (scintigraphy). Due to its low positron energy and short travel distance before annihilation, ^{18}F provides one of the best performances in PET system. ^{18}F has an half-life of 109.7 minutes and decays into stable ^{18}O via β^+ emission with a probability of over 96% with an energy of 0.633 MeV (Figure **2.5**). The average estimated positron range for this radioisotope ranges from 0.56 mm in water/soft tissue to 2.23 mm in the lung [12]. The production of ^{18}F is done with either cyclotrons or linear particle accelerators through bombardment of pure or ^{18}O-enriched water. [27]

Another well-known but less used radioisotope in PET imaging is Gallium-68 (^{68}Ga). It has a more complex decay than ^{18}F, having multiple and more energetic positron emission branches, with the total ratio being 88.88% and maximum energy being 1.899 MeV, although a shorter half-life of 67.7 minutes. There are also transitions to an excited state that will promptly, or within a few picoseconds, emit gamma photons, with a combined probability of 3% (prompt gammas) (Figure **2.5**). The ^{68}Ga positron range is estimated to be 2.62 mm in water and 9.94 mm in the lungs. [12] Although a former go-to radioisotope for cancer staging, specially of neuroendocrine tumors, its use nowadays is essentially related to infectious processes and chronic infections. [28] It's also much cheaper to produce and operate as it does not require a cyclotron, making it relevant from an economical point of view. ^{68}Ga is obtained from its parent radioisotope, Germanium-68, via Ge-68/Ga-68 Generators. However, current generator technology is not optimal for medical purposes. It offers low concentrations of ^{68}Ga and high probability of contamination with ^{68}Ge and metal ion impurities, [29], [30] which can prevent radiotracer labelling.
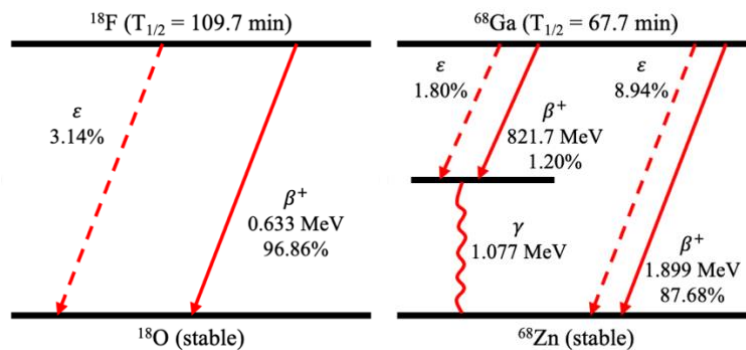
Figure 2.5: Decay scheme of 18F (left); Decay scheme of 68Ga (right). ε represents transitions by electron capture, γ represents prompt-gamma emission. Adapted from [31].

6

Carbon-11 (^{11}C) has been shown to be useful in PET imaging of prostate cancer, and other low-grade tumors, as an alternative to ^{18}F, [32] due to the latter's nonspecificity and the hypometabolic behavior of some tumors. It decays via positron emission with a branching ratio of 99.75% and an energy of 0.960 MeV, with a short half-life of just 20.4 minutes (Figure **2.6**). [32] The short half-life has limited this radioisotope's use in clinical settings. It is produced in cyclotrons from its parent radioisotope, nitrogen-14. [27] The mean positron range has been measured to be 1.03 mm in soft tissue and 3.98 mm in the lung. [12]

Nitrogen-13 (^{13}N) is one of the earliest discovered positron emitters, being discovered by Joliot and Curie, part of a research effort that awarded them the Nobel prize in Chemistry in 1935. ^{13}N is a short-lived radioisotope with a half-life of 9.97 minutes, a clear drawback for widespread use. It's considered to be a pure positron emitter as the branching ratio for the emission is almost 100% (Figure **2.6**). It has relatively high positron emission energy of 1.198 MeV and a mean positron range of 5.4 mm in water. Generally produced in multi-giga-becquerel cyclotrons via the ^{16}O(p,α)-^{13}N reaction, it is of quite limited use in clinical imaging. [33] Still, it is especially relevant in the cardiological field, particularly quantification of myocardial and coronary blood flow. [34], [35]
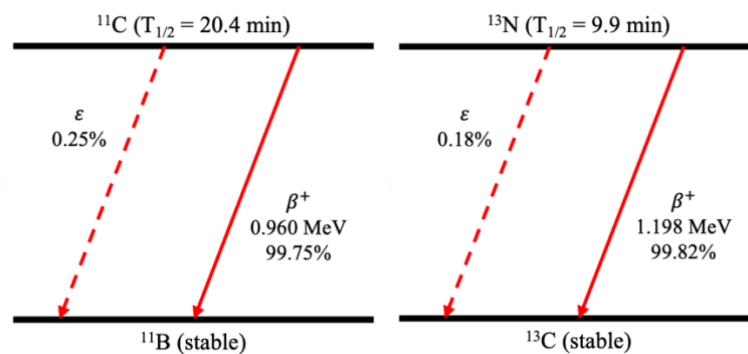
Figure 2.6: Decay scheme of ^{11}C (left). Decay scheme of 13N (right). ε represents transitions by electron capture. Adapted from [31].

Oxygen-15 (^{15}O) is an radioisotope with a very short half-life of just 2.1 minutes that is originated from ^{16}O in cyclotrons. Such a small half-life and the only means of production being via cyclotron meant great limitations for its usability, which led early researchers to dismiss it as a radiotracer for PET imaging. With the necessary resources, ^{15}O proved to be very useful for the diagnosis and study of cardiovascular diseases (e.g. coronary artery disease), as well as brain imaging (in vivo regional measurement of blood flow and volume). The positron branching ratio of 99,89% and the transition energy of 1.735 MeV (Figure **2.7**) give the positrons originated from this radioisotope a mean range of 2.44 mm in soft tissue and 9.26 mm in the lungs. [12]

Rubidium-82 (^{82}Rb) is a very high energy radioisotope nowadays commonly used for myocardial perfusion imaging and diagnosis of myocardial ischemia or coronary artery disease. It's decay scheme (simplified in Figure **2.7**) is a very complex one, with dozens of possible transitions between states. About 12 of them are β$^+$, of which the highest energy comes at 3.381 MeV with a branching ratio of 81,81%. In total, the positron emission probability is over 95%. [31] Additionally, there is a prompt-gamma emission with a combined ratio of 14.16%. [36] The positron range has been estimated to be 5.21 mm in water and 19.80 mm in the lung. [12] Although the production of ^{82}Rb is relatively simple and fast (in 10 minutes it is possible to produce enough quantity for 10-15 exams), done through Rb-82/Sr-82 generators, it has a very high cost which might not be sustainable in all hospitals or research centers. [37]
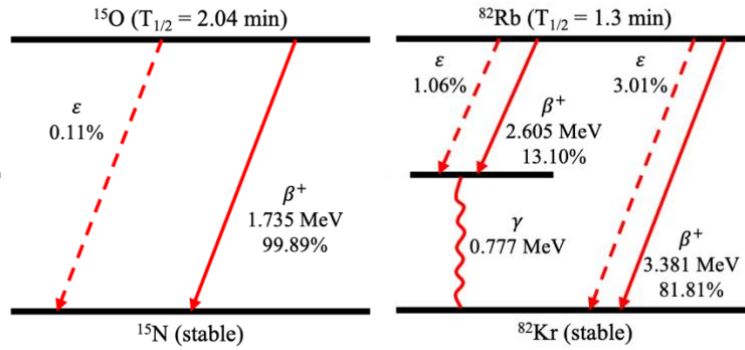
Figure 2.7: Decay scheme of ^{15}O. (right); Simplified decay scheme of ^{82}Rb (left). ε represents transitions by electron capture, γ represents prompt-gamma emission. Adapted from [31].

The need for cyclotron-based production of radioisotopes is a very limiting factor of PET imaging. Many times, radioisotopes are bought from third-party suppliers which already have methods of transportation with the necessary security measures in place. Still, transportation times and efficiency might prove very difficult or even impossible to more remote locations, especially for radioisotopes with very short half-lives. Fast transport by helicopter or plane is sometimes necessary (or preferable) but is not always available and its costs are unsustainable for many hospitals, universities and research centers. Although air transportation is the fastest way, there are still two stages of ground couriers (production site to origin airport, destination airport to PET facility), as well as security measures at the airport which can take up to two hours. For instance, for a 2h flight, the total shipping time will be over 5h, depending on the distance to the respective airports, which represents many half-lives of the radioisotopes (over 3 half-lives for ^{18}F) and implies the production of several times the needed activity, driving up the costs greatly. Even in cases where all these conditions are met, there is still a need for extensive planning and patient preparation, in order to avoid the cancellation of exams and wasting of money, time, and overall resources. [38]

Furthermore, due to the radioactivity, the transport needs to be regulated and controlled as to not expose bystanders to high levels of radiation and radioisotopes need to be transported in safe containers, by trained professionals who know how to properly handle and care for sensitive, perishable, hazardous materials.

2.1.3 Scintillation Detectors

PET imaging traditionally uses scintillating material coupled to photomultiplier tubes (PMT) for the detection of gamma photons emitted by the positron annihilation. This process comprises conversion of the 511 keV photons into visible light through interaction with the material, which can be divided in three main steps. At first instance, the photon interacts via Compton scattering or photoelectric absorption, creating a free electron in the material. As this electron travels through the material, it excites other electrons, losing its own energy. When the excited electrons lose their energy and go back to the ground state, they emit visible light photons (in some cases, ultraviolet photons are also emitted), which will be caught by the photocathodes of the PMTs. [39]

The efficiency of the crystals depends on the material's properties. A high light yield should be ensured, which is generally done by taking into account the material's effective atomic number (Z_{eff}), density and refraction index close to that of glass, to minimize losses between the crystal and the detector. Moreover, short rise and decay times are preferable as to improve the temporal resolution of the detectors. *Lutetium Yttrium Oxyorthosilicate* (LYSO) is one of the most used materials in PET systems, alongside *Bismute Germanate* (BGO) and *Sodium Iodide* (NaI).

The use of PMTs is important in PET for the amplification of the light signal originated in the scintillator into an electronically readable signal. As the photons emitted by the crystal hit the PMT's photocathode, electrons are released and go through a series of dynodes where they will be multiplied via secondary emission until they reach the anode, where the signal is read-out. This process is illustrated in Figure **2.8**. PMTs offer excellent gain and a high signal-to-noise ratio (SNR)

Over the last few years, other types of detectors for PET imaging have been tested and used commercially. Avalanche photodiodes (APD) and silicon photomultipliers (SiPM) are the two most popular alternatives to PMTs, both offering their respective advantages and drawbacks. This will be explored further ahead in this work.
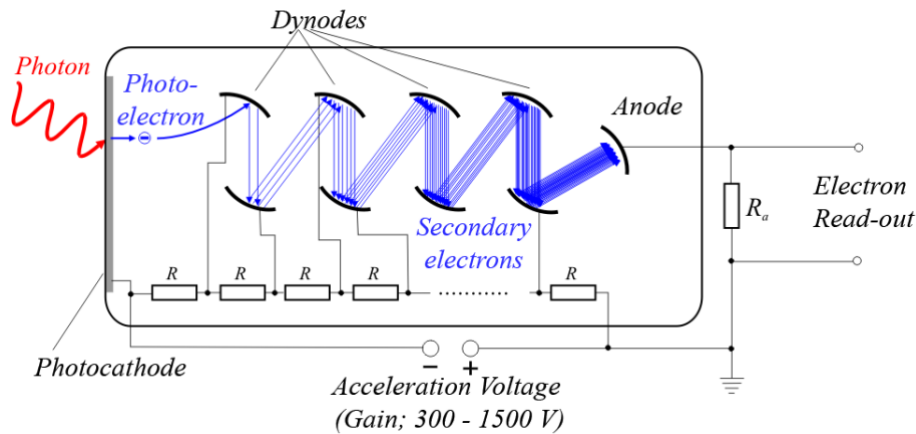
Figure 2.8: Scheme of the amplification of the light photon into an electronically readable output in a photomultiplier.

2.1.4 Interaction of Particles and Matter

When emitted by radionuclides, positrons are subject to a series of possible interactions with the atoms of the surrounding matter, annihilation being just one of them.

Elastic scattering, or Rutherford scattering, refers to the process where charged particles, such as positrons, are deflected by an atom's electromagnetic field created by the Coulomb potential, without any loss of energy. The positrons can be largely deflected or even backscattered while the atom remains unaffected. These interactions were first described by Rutherford, in an experiment represented in Figure **2.9**.
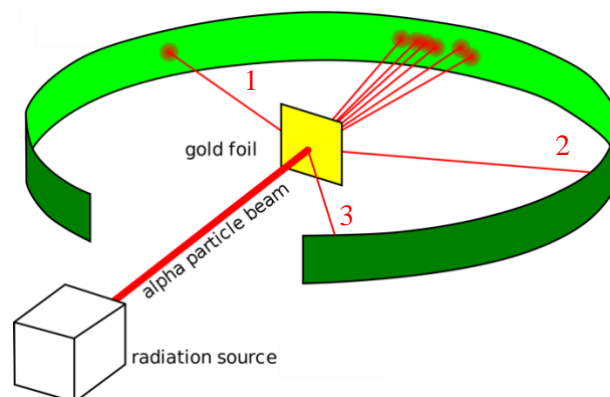
Figure 2.9: Representation of the Rutherford experiment. 1 and 2 represent large deflection angles, and 3 represents a backscattered particle. [40]

An inelastic scatter process takes place when the charged particle loses energy while interacting with the matter. This is the case in ionization and excitation of the atoms, by transfer of energy from the charged particles to the bound electrons, which will move further away from the nucleus to more energetic orbitals (excitation) or be ejected from it (ionization) if the energy of the particle is high enough. The transfer of energy determines the collision stopping power of particles. [41]

Bremsstrahlung, from the German "braking radiation", is a type of radiation originated when charged particles are abruptly slowed down and deflected by a close-by electrical field from an atom. Through conservation of energy, the loss in kinetic energy by the particle is converted into a photon, in this case an X-ray (Figure **2.10**). Because there is loss of energy, this effect is relevant to the stopping power, specifically it's radiative term.

Stopping power includes both the terms described above, collision and radiative stopping powers, also commonly referred to as hard and soft collision stopping power. Although it depends on many factors, such as the properties of the stopping medium and particle energy, [42] broadly speaking, it can be written that:

$$\frac{\left(\frac{dE}{dl}\right)_{rad}}{\left(\frac{dE}{dl}\right)_{col}} \propto EZ \tag{2.2}$$
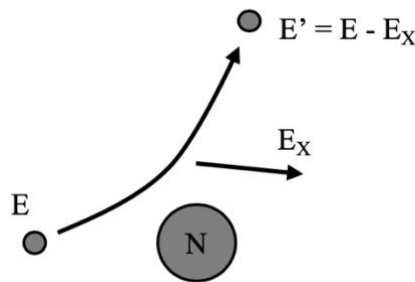
Figure 2.10: Representation of bremsstrahlung. When it is the deflected, the particle loses energy in the form of X-rays (E_X), slowing down.

As matter and its anti-matter cannot exist simultaneously, and positrons are the anti-particles of electrons, they cannot coexist. The laws of physics allow for a very limited number of possibilities for the outcome of a collision between these two particles. The creation of a pair of 511 keV gamma photons is the most probable result, given the conservation of linear and angular momentum, energy and electric charge. Generally, it is assumed that the photons are emitted in exactly opposite directions (180º). As described before (Figure **2.1**) this is the fundamental principle for PET imaging. However, when the net linear momentum of the pair is not null, the angle of emission is slightly altered.

After annihilation, photons are also susceptible to multiple kinds of interactions before reaching the detector, and even inside the detector, such as pair production, Compton and Rayleigh scattering, and absorption via the photoelectric effect. These interactions were represented in Figure **2.11**.
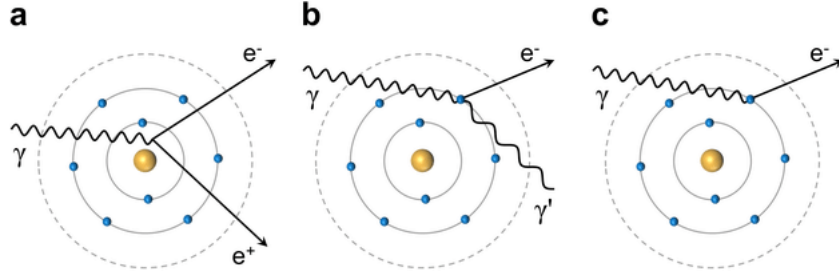
Figure 2.11: Possible photon interactions with matter. (a) Pair production. (b) Compton scattering. (C) Photoelectric effect. In the case of Compton scattering, the energy of the scattered photon (γ') is smaller than the original photon (γ). Adapted from [43].

Pair production is a process where a pair of electron/positron is created from the interaction of a photon with an electromagnetic field (Figure **2.11**(a)). Thus, due to the need of an external field and the conservation of momentum and energy, this process can only take place when in the presence of a third-party – usually an atomic nucleus. [44] Following Einstein's formula, this process can only take place when the energy of the photon is bigger than that of the electron-positron pair. As the positron is the electron's anti-particle, they have the same mass and thus the energy of the pair will be $2m_ec^2 = 1.022$ MeV. Pair production becomes especially relevant at high energies and in the presence of heavy nuclei, as its probability, or cross-section, is dependent on the energy of the photons and the atom's atomic number, according to Equation 2.3. [43]

$$\sigma_{pair} \propto Z^2 \ln\left(E_\gamma\right) \tag{2.3}$$

A variation of this process is internal pair production, where the electromagnetic field inherent to the nucleus, with an excess energy higher than 1.022 MeV, induces the ejection of an electron-positron pair without the intervention of an external photon. [45]

Compton scattering, also commonly referred to as inelastic scattering, comprises alteration of the energy, direction and wavelength of a photon that interacts with a weakly bound electron from the outer orbitals of atoms (Figure **2.11**(b)). The decrease in energy, which is transferred from the photon to the electron, called recoil electron, results in an increase in the photon's wavelength as described by the Compton formula, derived by Compton in 1992:

$$\Delta\lambda = \lambda' - \lambda = \frac{h}{m_ec}(1 - \cos\theta) \tag{2.4}$$

As such, the energy of the scattered photon depends on the scattering angle (θ) [46]. At high energies, the scatter angle tends to zero, meaning the scattered photon will barely be deviated from its original path and will behave like there was no scattering. Compton scatter does not depend on any property of the absorbing material. [47]

Rayleigh scattering, or coherent scattering, is only relevant for low energy photons (<< 50 keV) and is a type of elastic collision, meaning the scattered photon has the same energy as the incident photon. This interaction occurs between photon and atoms in their entirety, as opposed to interaction with electrons. Rayleigh scattering shows a strong dependence on the photon's wavelength:

$$\sigma_{Rayleigh} \propto \frac{1}{\lambda^4} \tag{2.5}$$

Rayleigh scattering is never the dominant process in interaction of photons with matter and is of little to no importance in nuclear medicine and, particularly, PET imaging.

The photoelectric effect is a type of interaction described by the total absorption of a photon's energy by an atom. When the energy of the photon (E_0) is equal to the binding energy of the electron shell (K_B), a photoelectron is ejected. When the energy of the photon is higher, the surplus is converted into kinetic energy of the photoelectron (K_{pe}).

$$E_{pe} = E_0 - K_B \tag{2.6}$$

The ejection of the electron creates a vacant spot in the orbital which will be filled by an outer orbital electron. When the outer electron moves from one orbital to the other, there is an emission of characteristic X-rays, also referred to as Auger electrons, with an energy of only a few keV that corresponds to the difference of energy between the orbitals. [47] Contrary to Compton scatter, the photoelectric effect shows dependence on the material, as well as on the energy of the photon:

$$\sigma_{PE} \propto \frac{Z^2}{E_\gamma^3} \tag{2.7}$$

The dominance of each type of interaction is dependent on both the atomic number of the interacting material and the energy of the photon, as shown in Figure **2.12**.
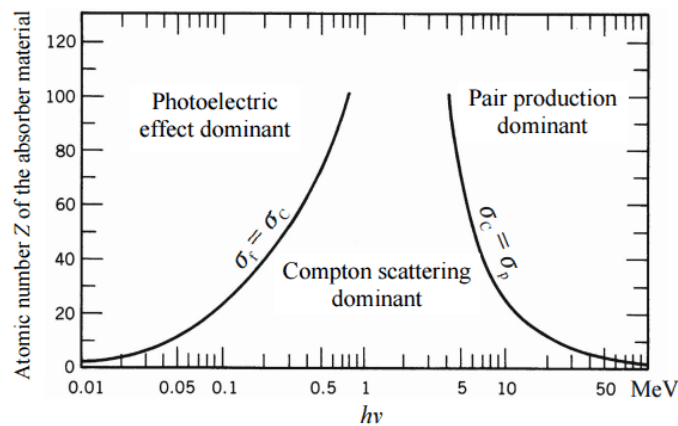
Figure 2.12: Dominance of effects according to photon energy and atomic number of the material. Rayleigh scattering is not represented as it is not significant for PET imaging. [48]

2.2 Magnetic Resonance Imaging (MRI)

Magnetic Resonance Imaging (MRI) is one of the most advanced, complex and versatile imaging techniques there is nowadays. It allows for both metabolic and anatomic information of the body, with great soft tissue sensitivity and contrast, without the use of ionizing radiation. In addition, it is a 3D technique that allows for the simultaneous imaging of multiple planes of the body, eliminating the need for translation of the patient inside the scanner.

MRI is based on the phenomenon of nuclear magnetic resonance (NMR). When an atom's nucleus is composed of an odd number of protons or neutrons, it will exhibit a property known as *spin*, which, for simplicity, can be thought of as the rotation of the nucleus. As it is positively charged, the rotation will induce a small magnetic field around itself. Left undisturbed, the tissue's nuclei will be oriented in random directions, cancelling out any collective magnetic effect. However, when subject to a stronger, external magnetic field, B_0, the axis around which the nucleus rotates will tend to align with the direction

of B_0, never fully reaching it and continuously precessing around that axis, in a parallel or anti-parallel direction, with a frequency ω called the Larmor frequency (

Figure **2.13**).
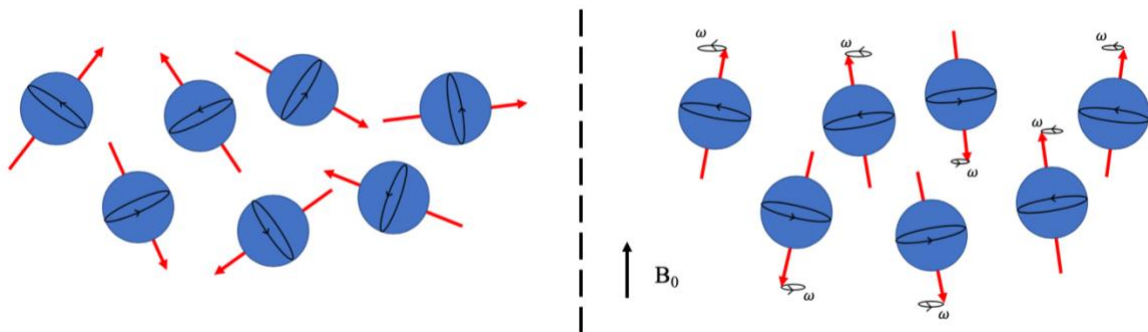
Figure 2.13: Free atoms with intrinsic spins in random directions (left). Atoms precessing at the Larmor frequency ω around the magnetic field's (B0) direction (right). Adapted from [49].

The Larmor frequency is dependent on the strength of the magnetic field, as well as other nuclear properties that are condensed into the gyromagnetic ratio, γ. As the energy of the parallel direction is slightly lower than the anti-parallel, it will be favoured, and a non-null magnetic effect (bulk magnetization) arises in the direction of the magnetic field. Because the spins are out of phase with it each other, the bulk magnetization will have no transversal components and will be aligned with the B_0 axis. By applying radiofrequency (RF) pulses, which are alternating magnetic fields with frequency equal to the Larmor frequency, the magnetization is forced to tip over and a transversal component is induced (Figure **2.14**), and the spins will be in phase. Stopping the RF pulse will cause the spins, and thus magnetization, to return to its initial direction, in what is called Relaxation. Relaxation comprises two independent mechanisms: spin-spin and spin-lattice interactions. [50]
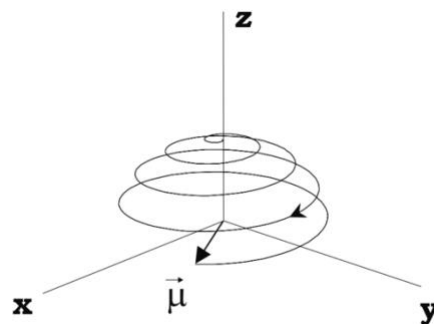
Figure 2.14: Tipping over of the net magnetization ($\vec{\mu}$)caused by the application of and RF pulse. [50]

Spin-lattice interactions result in the recovery of M_z after the application of the RF pulse through the realignment of the spins with B_0, by exchanging energy with the surrounding tissue. Mathematically, this recovery is modelled by an exponential curve and its growth constant being T1 (*spin-lattice relaxation time*), the time it takes for M_z to recover 63% of its initial value (Figure **2.15**). [50]

Spin-spin interactions are the de-phasing of spins after the RF pulse is stopped and result in a decrease in the transversal component of the magnetization (M_{xy}) as it returns to the original state. This is described by an exponential curve with a time constant T_2 (*spin-spin relaxation time*), which represents the time it takes for M_{xy} to reach 37% of its original magnitude (Figure **2.15**) and depends on the tissue type, as well as being affected by inhomogeneities in the magnetic field. [49]

13
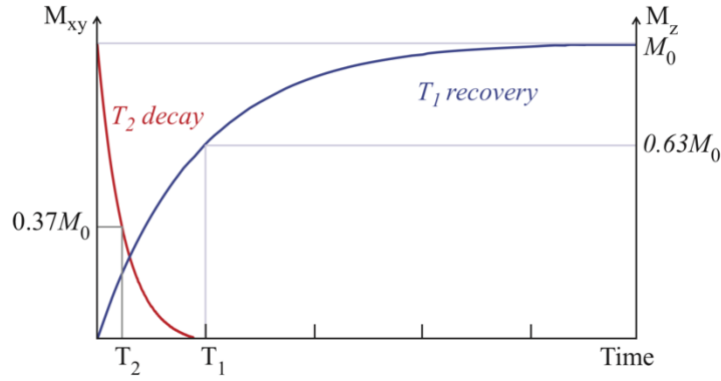
Figure 2.15: Graphical representation of T1 and T2 relaxation. T1 and T2 are constants measured for 90° RF pulses. [51]

To allow for the imaging of the detected signals, special encoding is still needed in order to precisely locate where the signals are coming from. This process is done in three parts: slice selection, frequency encoding and phase encoding.

A slice is selected by introducing a linear gradient in the magnetic field in the axial direction (Figure **2.16**). As mentioned before, the frequency of the spin is proportional to the strength of the magnetic field. In the presence of a gradient, spins in different location are subject to different strengths, and the RF pulses with the Larmor frequency corresponding to those strengths will only induce magnetization in a specific part of the patient's body, selecting a slice and locating the origin of the signal in the axial direction, giving it a z coordinate, G_z.
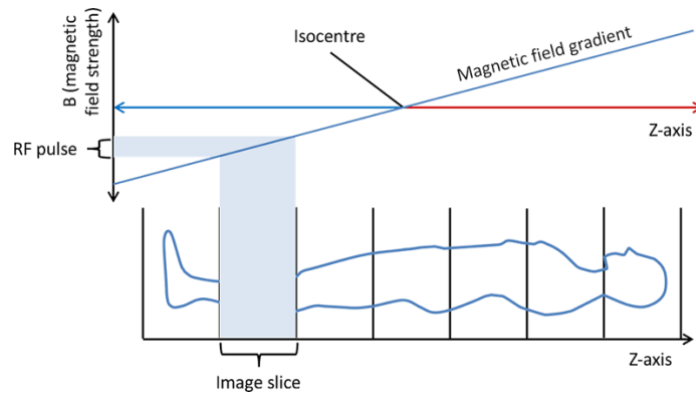
Figure 2.16: Principle of slice selection through the application of a linear magnetic field gradient and a small bandwidth of the RF pulses. [52]

To further locate the spins, the same principle is applied in the y and x directions, with a *phase encoding gradient* and a *frequency encoding gradient*, respectively, all at different times. The three successive gradients then yield all the necessary coordinates (G_x, G_y, G_z) to precisely locate the spins. This information is then stored along with the time in a 4D spatial frequency domain called the k-space. [53], [54] By applying an inverse Fourier transform to this domain, the MR image is formed.

There is a large number of sequences that offer different contrasts between tissues, with different applications and purposes. Different sequences are achieved by selecting different RF pulse duration, intensity and shape, as well as the interval between them. The combination of this selection leads to very different image properties and different contrasts. MR image reconstruction and sequences are a matter that falls out of the scope of this dissertation and will not be discussed further.

2.3 PET/MR Hybrid systems

There are many approaches to multimodal imaging, involving different processes (simultaneous or sequential) and, of course, different techniques. The combination of different techniques provides many advantages, one of the biggest ones being that it joins physiological information with anatomical information, allowing for a better understanding of the human body and many kinds of diseases (cardiological, oncological, etc). PET/CT is nowadays one of the most popular multimodal imaging techniques, with thousands of systems installed worldwide. However, over the last few years, PET/MR has been gaining more and more popularity.

The idea of creating a fully integrated whole-body PET-MR hybrid system was proposed in the 1990s. [55] Since the insurgence of this concept, several studies have been conducted in order to make the differences between both systems compatible, both hardware- and software-wise. [56] In recent years, this kind of system has become commercially available, [57], [58] giving way to many studies regarding the potential of this multimodal technique.

The development of integrated PET/CT systems was quite straightforward, simply involving mounting stand-alone systems in a common gantry as there are no major incompatibilities. However, the process for PET/MRI was quite more troublesome and complex. The presence of the magnetic field, the size of both systems, the PET's need for linear attenuation coefficients, which are obtained directly from CT scans but not MRI, full integration with the same FOV, among others, are technical challenges that had to be overcome in order to build integrated PET/MR systems.

Traditional PET detectors are usually made of inorganic scintillation crystals, *lutetium oxyorthosilicate* (LSO) or LYSO being the most used, coupled to photomultiplier tubes (PMTs). The magnetic field causes the electrons to deviate from their original path, causing tremendous loss in gain and rendering PMTs essentially useless in magnetic field of several mT. [59] Therefore, the main challenge was to find a way to have both systems operate simultaneously or at least in close proximity, like PET/CT scanners, which operate in-line, with the patient going through the CT before being in the FOV of the PET scanner. The crystals themselves are largely unaffected by the magnetic field and have also been shown to have little to no impact in MRI images [60] and so, the challenge relies mainly on replacing PMTs or changing the way they are coupled to the detectors. Besides the magnetic field issue, the size of the detectors would also have to be significantly decreased, to allow them to be placed inside the MRI bore without reducing the diameter so much that a patient could not fit inside. With the photodetectors being placed inside the MRI, the electronics associated with them will also have to be inside and thus, the circuit layouts, choice of components and good RF shielding have to be carefully chosen in order to avoid multiple kinds of interference and artifacts between both systems.

In early stages, the focus was mainly on separating the detector crystals from the PMTs and coupling them via fiber optics, placing all the PMTs in a magnetic field free environment. This solution was very impractical and raised many problems, such as the handling of such a large quantity of fiber optics and poor energy and timing resolutions. (Figure **2.17**)
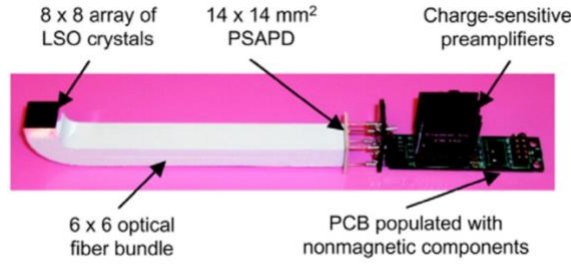
Figure 2.17: PET detectors coupled via fiber optics. [56]

The focus then shifted to the development of a new generation of detectors that could replace PMTs and perform well under magnetic fields. Avalanche photodiodes (APDs) and silicon photomultipliers (SiPMs, also known as Geiger-mode APDs) both fulfill almost the necessary requirements, being unaffected by strong magnetic fields and having an internal gain suitable for the purpose. Even though APDs have some good qualities, they have not been widely used in clinical PET systems due to its sensitivity to temperature and voltage, as well as the poor temporal resolution. Compared to APDs, SiPMs have a much higher gain at much lower voltages, providing a high SNR without the low-noise front end electronics. Their speed provides these detectors with very good temporal resolution, comparable to that of PMTs, although their characteristics (smaller sensitive area) result in a lower photon detection efficiency. More technical detail on both types of photodetectors is shown in Table **2.1**.

Table 2.1: Comparison of different types of photodetectors used in PET/MR systems.

	GAIN	BIAS VOLTAGE	SIZE	EFFICIENCY	TEMPORAL RESOLUTION	COST
PMT	10^6	$800V - 1kV$	Large	~ 30%	< 600 ps	High
APD	10^2	$100V - 1kV$	Small	~ 80%	~ 1 ns	Medium
SIPM	10^6	30V	Small	< 40%	~ 100 ps	Low

2.3.1 Effect of the Magnetic Field on Positron Range

As stated previously, when a positron is emitted by a radioisotope, it travels some distance in the tissue before it annihilates with an electron and forms a pair of 511 keV photons. With no restrictions, the positron emission is generally considered to be isotropic. However, from quantum physics it is known that when submitted to a magnetic field, $\vec{B}$, charged particles (such as positrons) will be induced in a helical trajectory along the direction of the magnetic field due to the Lorentz force, $\vec{F}$:

$$\vec{F} = q\vec{E} + q\ \vec{v} \times \vec{B} \tag{2.8}$$

where q is the charge of the particle and $\vec{v}$ is its velocity vector.

This helical pattern results in shortening of the transversal range, with no significant alteration in the axial direction (Figure **2.18**). From this, knowing that typically the magnetic field in an MRI system is along the z-axis (axial), we can expect increased resolution in the x- and y-axis (transversal), and either no difference or a decreased resolution in the z-axis. Although the range of the positron range in the axial direction is not significantly changed, the profile (distribution) of the particles is much elongated. Physics also predicts that the effects are greater the higher the energy of the positrons.
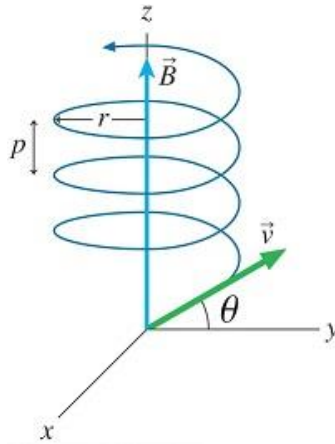
Figure 2.18: Helical path of positrons subject to a magnetic field. [61]

From the time this effect was proposed, these predictions have been confirmed by experimental studies. Hammer and Christensen [10] determined that for Galium-68, the positron range in the direction transversal to the magnetic field is significantly reduced, predicting that this would consequently reduce image blurring if an image was to be reconstructed out of the measurements (their data was simply analytical). Studies using Monte Carlo simulations also lead to the same conclusions – transversal positron range is reduced under static magnetic fields. [16], [62] It has also been shown that the effect is greater the stronger the magnetic field is, i.e., positron range is reduced further when the strength of the magnetic field increases, while the non-collinearity remains untouched. Furthermore, it concluded that the effect of magnetic fields is also dependent on the energy spectrum of the emitted positrons, showing barely significant improvements in resolution for ^{18}F but great differences for ^{68}Ga. A study carried out by Shah et al in 2014 [14] is one of the few that uses realistic phantoms (in this case, brain phantom) and studies the effect of magnetic fields in both point sources and reconstructed PET images, analyzing the results for all directions and for low, medium and high energy radioisotopes. In the reconstructed images, the effect of the magnetic field becomes very clear (Figure **2.19**). High energy radioisotopes such as ^{120}I are greatly affected by the magnetic field, resulting in a significant improvement in transaxial spatial resolution, while low energy radioisotopes such as ^{18}F showing little to no improvements. In the study with the realistic brain phantom, there was significant increase in both resolution and contrast from 3 T magnetic field and stronger (7 T and 9 T), especially for ^{68}Ga and ^{120}I.
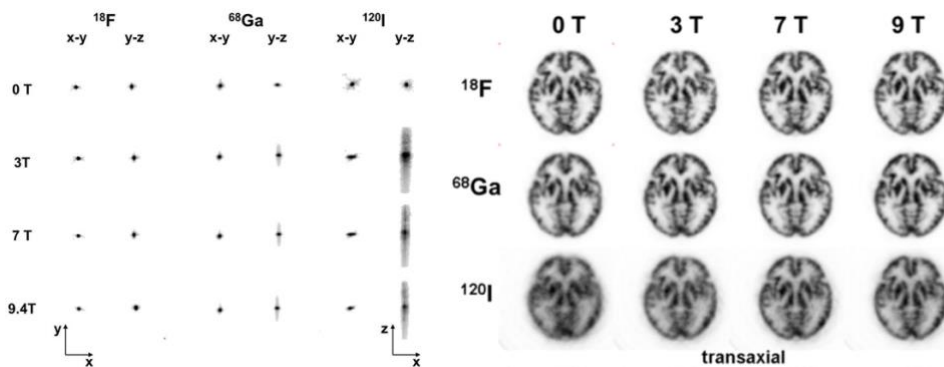
Figure 2.19: PET/MR images of a point source (left) and brain phantom (right) filled with different emitters at different magnetic field strengths. [14]

Overall, results seem to be consistent in all studies, always reaching the conclusion that a magnetic field will reduce the positron range in its perpendicular directions, while not significantly affecting the axial directions, allowing for a better spatial resolution and contrast on the transversal plane. Despite the axial positron range not being affected by the magnetic field, some studies have found that certain artifacts are introduced in PET-MR images. One of the most significant ones is the shine through effect

(Figure **2.20**), [15] where there is an apparent additional uptake of high energy radiopharmaceuticals in areas across an air cavity from the real place of injury. This artifact is a consequence of the elongation of the positron range in the direction of the magnetic field, combined with the current algorithms for PET-MRI image reconstruction. It can be very misleading because there are apparent lesions that may appear to be bigger or more significant, i.e., sometimes the artifact area is brighter than the actual lesion, possibly inducing professionals into a wrong diagnosis or diagnosis of lesions in wrong places. Other artifacts have also been studied, namely ones from off-plane sources, where the conclusions were that the artifacts are much sharper at high magnetic fields, instead of a diffuse background blurring. Furthermore, it was shown that these artifacts can be almost completely eliminated in simple source configurations by correcting positron range in the reconstruction algorithm, although for complex sources the problem persists. [63]
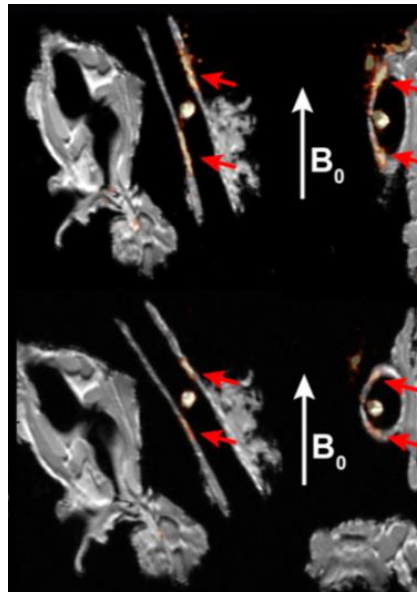
Figure 2.20: Shine through artefacts on PET/MR images at 20º (top) and 35º (bottom) angles. [15]

2.3.2 Total-Body PET/MR

With today's radiation dose and administered activity regulation and state-of-the-art PET scanners, it is impossible to images with high SNR values in short acquisition times. Even in the most sophisticated scanners, sensitivity is relatively low (less than 1%), given that roughly 90% of the body is outside the scanner at all times, making it impossible to obtain coincidences from most of the body. Furthermore, for the portion that is covered by the detectors, only about 5% of the signal is registered because of the isotropic emission of the gamma photons. Both these problems can be addressed in a very simple manner: extending the length of the scanner to cover the whole body and significantly increase the acceptance angle of photons. This is exactly what Simon Cherry and Ramsey Badawi et al did with the EXPLORER scanner. [18] Their predictions indicate a 40-fold increase in sensitivity, which can be translated into multiple advantages from a scanning point of view: greatly increase SNR to improve image quality and possibly detect smaller and lower-contrast structures, significantly reduce (by a factor of 40) the scanning time to just a few seconds while maintaining the current state-of-the-art image quality and SNR, or reducing the injected activity by a factor of 40.

From allowing PET scanning to be used for sensitive populations such as children, significantly improving patient throughput in high-demand clinics, or reducing operational costs by using much less activity, the possibilities for this kind of scanner are very diverse and can be looked at from many points

of view. It also opens the door for multi-tracer studies and total-body dynamic imaging and kinetic analysis. [64]–[66]

Although the integration of a total-body PET with MRI would be technically possible, even with its fair share of technical challenges, this is only a dream for the near future. Even though total-body MRI protocols are available, they are not widely spread and their use within a total-body scanner would not be as advantageous as they require translation of the patient, which would interfere with the PET acquisition. Furthermore, it would significantly increase the costs, which are high enough for a total-body PET system alone and are a concern for the inventors regarding the adopting of these scanners in clinical context.

3 NEMA Performance Measurements of Positron Emission Tomographs

In this chapter, the National Electrical Manufacturers Association (NEMA) performance measurement tests for PET scanners are described. It covers the different tests performed in this dissertation, as well as additional ones commonly performed.

In order to reliably compare PET and PET/MR scanner's performances amongst different models, it is necessary (or at least recommendable) that all manufacturers follow the same set of guidelines for testing of their scanners. The National Electrical Manufacturers Association (NEMA) is an American organization that represents hundreds of electrical and medical equipment manufacturers. Although NEMA is not a regulatory entity, it does lobby for the safety, reliability, efficiency and cost reduction of all kinds of electrical equipment and medical imaging systems in the US. In addition to lobbying, NEMA regularly publishes and updates hundreds of standards and other documents that are used as guidelines for device testing, which throughout the years have become a worldwide standard for characterization of electrical and medical devices.

The NEMA Standards Publication NU 2-2007 [67] is a document that provides the procedures to perform the necessary measures to characterize and classify PET scanners. The publication includes many different tests, such as spatial resolution, sensitivity, scatter fraction, count losses and randoms measurement, and image quality, which will be described below.

It is important to point out that these tests are currently only done with ^{18}F and are optimized to that radioisotope only. Furthermore, they are set for the currently commercially available PET/MR scanners, which short AFOVs, which are not suitable for the study of total-body, next generation PET scanners and must be adapted in the future to allow for a better understanding of these scanner's scanners' performance, and also to have a reliable way of comparing them to the current generation of scanners. With the increase in number and usage of different radioisotopes for more specific examination, adaptation of the procedures to include other radioisotopes, such as the ones mentioned in Section 2, is mandatory in the future. This will be discussed further in this dissertation.

3.1 Sensitivity

Sensitivity measures a scanner's efficiency in obtaining coincidence data and is usually measured in counts per seconds per kilo becquerel (cps/kBq) and can be thought of as the fraction of decays that is registered by the detectors. It depends greatly on the geometry of the scanner (geometric efficiency) and also on the detection efficiency intrinsic to the detectors (intrinsic efficiency). The geometric efficiency is dependent on the width and length of the scanner, more specifically on the detectable solid angle, inside which coincidences can be detected. Intrinsic efficiency is mainly related to the properties of the detectors, mainly the atomic numbers of its components. The sensitivity test for PET scanners is performed with very low levels of activity spread out throughout a 70 cm plastic tube, to ensure minimum count losses and minimise the effect of dead time. Successive measurements are taken, adding a layer of attenuating material (aluminum) between each scan (Figure **3.1**, left). The tubes are positioned parallel to the axial direction and are held in place by a phantom holder Figure **3.1** (right), to minimize movement of the source between each scan. The procedure is repeated two times, at different radial

positions: at the center of the FOV and with a 10 cm offset from the center. The attenuation-free sensitivity is obtained later in post-processing, by extrapolating the value from the multiple attenuated measurements.
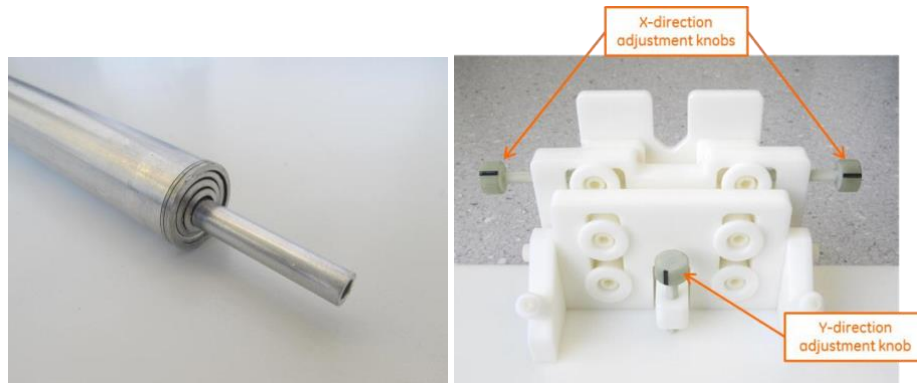
Figure 3.1: Left: Plastic tube (center) with surrounding aluminum cylinders. Right: Phantom holder. [67]

3.1 Scatter Fraction, Count Losses, and Randoms Measurement

The scatter fraction, count losses and randoms measurements, also referred to as count rate statistics test, are obtained from a single test that aims to calculate a system's ability to measure high-energy sources, and to recognize scattered radiation, as opposed to radiation coming directly from the positron annihilations. Peak NECR and the activity at which it occurs is one of the most important sets of data that comes out of this test, due to its relationship with clinically relevant data. Generally speaking, the higher the NECR, the lower the dose a patient has to be exposed to. NECR measures the true coincidences that are registered by the scanner, as compared to the total registered coincidences, which include scattered and random coincidences [68]. This test is performed overnight with a scatter phantom, a long, 70 cm polyethylene cylinder through which a 70 cm line source runs all through its height, 4 cm below the center (Figure **3.2**). The scatter phantom is positioned parallel to the axial direction of the scanner and the line source is filled with very high levels of activity (close to 1 GBq). Successive measurements are obtained periodically to measure each rate (total prompts and true, random and scattered coincidence rates) for multiple levels of activity, in order to plot the rates against the activity concentration.

Figure 3.2: Scatter phantom. [67]

3.2 Spatial Resolution

Spatial resolution (SR) is defined as the ability to distinguish between two points in the final, reconstructed image. The reconstruction should be done with no post-processing, such as smoothing or

apodization. Resolution can mean both Full Width Half Maximum (FWHM) and Full Width Tenth Maximum (FWTM), so it is important to clarify which one is being referred to. It is usually measured in millimeters. In both cases, the values are obtained through linear interpolation of the values of adjacent pixels corresponding to half or a tenth of the maximum value of the image's point spread functions. SR is determined in all directions, through radial, tangential and axial slices. For this test, glass capillary tubes with sub-millimetric internal radius and length such that the activity is not spread out for more than 1 mm are used. A dedicated phantom that holds the capillaries in precise coordinates is shown in Figure **3.3** (left). The test is performed at the center of the FOV and repeated at ¼ of that distance (Figure **3.3**, right).
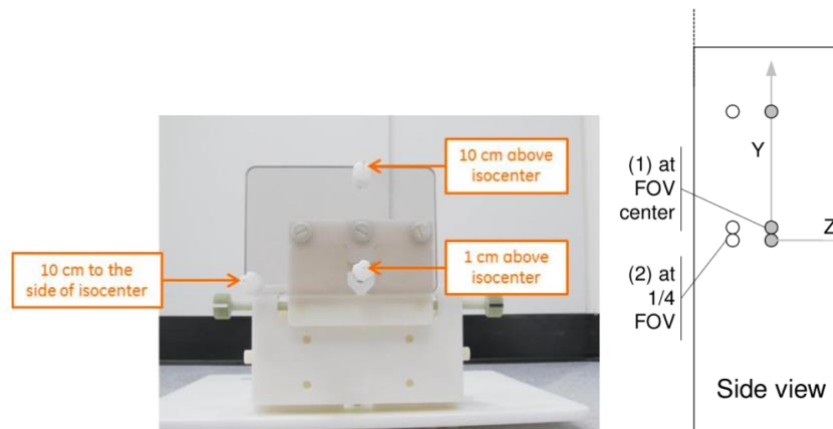
Figure 3.3: Spatial resolution phantom holder (left); Location of sources (right). [67]

3.3 Image Quality

Image quality is measured from a test that aims to simulate the whole body. It used two phantoms: a body phantom that simulated soft tissue, hot and cold lesions and lung tissue (Figure **3.4**) and the scatter phantom used previously (Figure **3.2**). The body phantom is composed of a large volume of water (background), and spheres of varying sizes (10 to 27 mm), with a central cylinder filled with foam beads to simulate lung tissue. Coupling the scatter phantom to the body phantom the test becomes more realistic, as the scatter phantom simulates the scattered radiation that comes from body parts that stay out of the scanner while performing the examination. This test measures the contrast recovery ratio (%) between the spheres and the background, as well as the background variability (%).
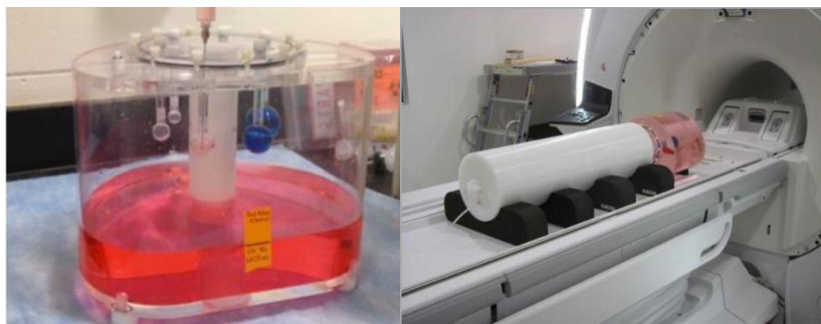
Figure 3.4: body phantom (left); phantom setup on the scanner bed (right).

In this dissertation, the NEMA measurements of sensitivity and scatter fraction, count losses and randoms measurement tests are used to compare the performance of different scanners, as well as the performance of a single scanner with and without the presence of an MR field.

4 GATE Monte Carlo Simulations

In this chapter, the reader is introduced to Monte Carlo methods, as well as GATE, the software used in this dissertation to perform simulations of the tests described in the previous chapter.

Monte Carlo methods are a set of algorithms designed to numerically solve differential and integral equations through the random sampling of variables from a probability distribution. They are used in all fields, from accounting and finance to engineering and astrophysics.

For probability calculation, the method can be explained in a simple manner, by imagining a situation where a coin is tossed a number of times, and each time the outcome is recorded simply as heads or tails. By the Law of Large Numbers, which states that "as the number of identically distributed, randomly generated variables increases, their average approaches their theoretical means", as the number of coin tosses increases, the obtained (simulated) probability value will be closer to the real value. In this case, it will be 0.5, as demonstrated in Figure **4.1**.
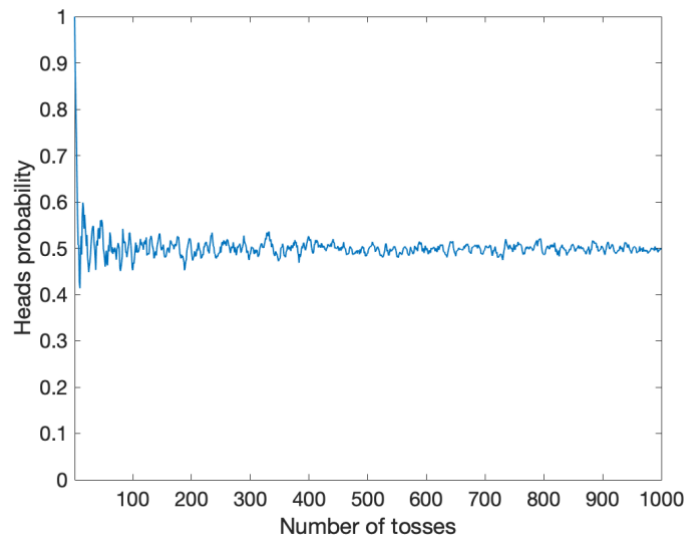
Figure 4.1: Probability of outcome being "Heads" when a coin is tossed a number of times. The greater the number of tosses (experiments), the closer the probability gets to 0.5.

For high energy particle physics, the principle of Monte Carlo simulations is the same. Each particle is in constant interaction with matter and other particles that surround it, and is susceptible to change its energy, direction, etc. These changes all have their own probability distributions, from which each parameter is randomly sampled in order to estimate the evolution of the particle, and are also dependent on the type of interaction a given particle can be subject to, as described before in Section 3.1.4.

4.1 GATE

Every simulation performed in this project was done using GATE – GEANT4 Application for tomographic Emission. GATE is an open-source software developed by multiple internationally recognized research groups with the aim of performing numerical Monte Carlo simulation regarding biomedical imaging and radiotherapy. [69] GATE is based on GEANT4, a toolkit developed at CERN

for the simulation of particles of all energies passing through matter, which has application is fields from astrophysics to medical imaging [70], [71] and is one of the most known and spread out toolkits for Monte Carlo simulations in particle physics.

Although there is an interactive mode, in which the user must enter commands one by one into the GATE command line, the simplest and best way to work in GATE is through macro files, which are ASCII files with '.mac' extension that contain command scripts. The use of scripting mechanisms eliminates the need for C++ programming, a key aspect of the development of GATE. It is common to write a main macro file which contains commands calling other macro files, these being responsible for the different setup steps such as scanner geometry, radioisotope source, etc. This modular way of creating a simulation allows for the possibility of re-using macro files across several simulations, avoiding the need to continuously repeat code within every macro, besides one line calling said macro.

4.1.1 Geometry and Materials

To build the scanner geometry in GATE, the software offers a set of templates with predefined geometries which can be adapted at will to model almost any desired system. These templates are described in tree level structure, with already some presets or assumptions made about the system type chosen by the user. For PET systems, GATE uses the 'cylindricalPET' system, which has 5 different hierarchy levels:

1. rsector (repeated n times with a ring repeater in order to cover the complete scanner bore)
2. module (represents one individual ring of the scanner)
3. submodule (the detector unit of the scanner that contains the sensitive crystals)
4. crystal
5. layer

Visual representation of the scanner geometry can be seen in Figure **4.2**. The output level is set later on the digitizer settings (section), when the readout depth is specified (the level at which the output is collected – usually crystal or layer).
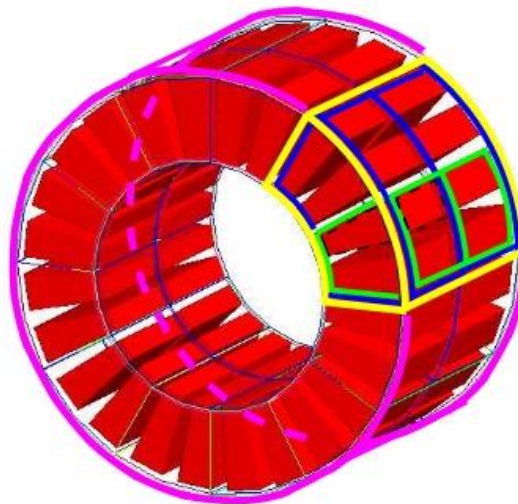
Figure 4.2: CylindricalPET in GATE. Pink: scanner cylinder; Yellow: rsector; Blue: module; Green: Submodule; Red: Crystal. Layer level not shown. [72]

While defining the scanner geometry, the materials from which each portion of the scanner is made is also defined. The materials are defined in a separate database file ("GateMaterials.db"). In this database, elements are defined as in the periodic table, containing information about each element's name, symbol, atomic number, and molar mass. Complex materials or molecules are defined based on

combinations of elements. To define a material, the user needs to specify its name, density, constituent elements and their respective abundances by mass fraction. To define a molecule or chemical compound, instead of element abundance, the number of atoms is specified. [73]

4.1.2 Physics

The physics macro is where the user defines all the physical processes taken into account by GATE for the simulation. For PET imaging, one should include all possible effects that may occur in the scanner to all particles involved – positron, electron and photon interactions (as described previously in Section 3.1.4). For the scope of this dissertation, all the discussed interactions were included in the physics macro and no energy cuts were made. Furthermore, GATE allows for the introduction of a magnetic field, although it has some limitations. The magnetic field can only be applied to the whole simulated world. It must be static and have the same strength throughout the world, meaning there are no gradients as in MR systems.

4.1.3 Digitizer

In GATE, the digitizer simulates the behavior of the scanner detectors and its signal processing chain, from the particle detection in the sensitive crystal to sorting out coincidence data. There are multiple parts that make up the digitizer, simulating the different steps of the signal processing chain in a real scanner.

PET detectors measure each hit in the crystal as a single pulse with a certain intensity, disregarding the energy difference in energy from the moment it first interacts with the crystal until them moment it is absorbed via photoelectric effect. Considering GATE has the ability of recording the entire history of a particle, from its emission to its absorption in the detector, the first stage of the digitizer is the adder. The adder sums up all the energy from a particle from the moment it first interacts with the crystal until it is stopped (until it is absorbed into the crystal via the photoelectric effect), taking into account the multiple interactions might occur within the crystal (e.g. multiple Compton scatter events).

Once a hit is recorded, a timing window called the coincidence window is open (Figure **4.3**). Within this period, the next hit that is recorded by another detector, located a minimal distance from the original one, is assumed to be a photon that originated from the same annihilation event. If the distance between detectors is too small, they are not registered as a coincidence because it would be physically impossible for both photons originated in the annihilation to be located so close together in the scanner bore. For this purpose, a minimum difference between sectors is defined with the *minSectorDifference* command. It is important to point out that the detected coincidence cannot yet be considered as a true coincidence, it might also be a scattered or random event.
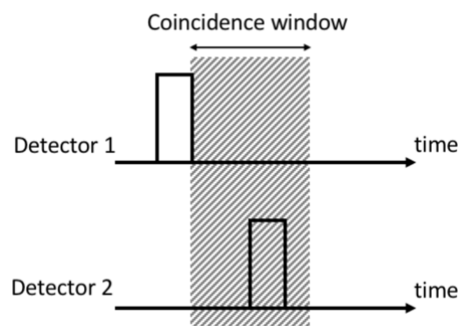
Figure 4.3: Illustration of the coincidence window principle. The event recorded in Detector 2, although considered a coincidence, can still be true, random or scattered event.

Furthermore, when more than two singles are in registered within the timing window, GATE will only record them as Coincidences according to the chosen multiple coincidences policy. The software offers a broad choice of policies. For this project, the default option, *keepIfAllAreGoods* was selected. This means that all the multicoincidences (coincidences composed of more than 2 singles) will be registered as long as they satisfy the previous conditions of being separated by at least the *minSectorDifference*.

Dead time of the detector is also modeled on the digitizer. Due to the physics of the detectors, they require a minimum time to detect an interaction with a particle, as well as time required by the electronics to register such an interaction as a hit. There are two ways of dealing with incoming particles during this timing window. On one hand, they can be discarded, only making the system available to process another hit after the previous one is completely finished. This is called non-paralyzable behavior. On the other hand, paralyzable behavior allows the system to stay sensitive to new hits and will pile them up, which may distort the signal and lead to loss of information from both events. However, at high count rates (high activities), the system will become saturated and it will not be able to register new hits. The counting behavior is characterized by the dead time. [74] The total dead time of a system comprises all dead times of the components, from the crystals to the electronics and processing, which makes it hard to determine precisely and, thus, simulate.

4.2 ROOT

ROOT is a powerful software kit developed by CERN for the handling and statistical analysis of large sets of data. In addition to saving, accessing and processing data, it has powerful graphical capabilities that can be adjusted interactively, in real time. ROOT files ('.root') are organized in a tree structure, with 'leaves' as subsets, that can be extremely quickly and efficiently accessed, allowing users to easily process the needed data. The software is mainly implemented in C++, also offering a seamless integration with R, python and Mathematica and allowing for a cross-platform analysis with the most advantages from each software. [75]

GATE offers a native ROOT output with several presets for each type of simulated system. For PET systems, the file consists of three main trees: Coincidences, Singles and Hits, in which a wide variety of variables are stored, such as position and energy of the particles. [76]

In this dissertation, GATE is used to build realistic models of a state-of-the-art scanner, the GE Signa PET/MR, as well as a conceptual design for a total-body PET scanner and perform the NEMA performance measurement tests of sensitivity and count rate statistics as described on the previous chapter. Furthermore, the software is used to perform a study of positron range in different tissues, without the need for scanner geometry.

5 Methods

In this Chapter, the experimental methods used to achieve the dissertation's aims are explained. A comprehensive description of the GE Signa and TB-PET geometries is presented, as well as the geometry of the NEMA scatter and sensitivity phantoms. The methods for data analysis for each of the tests are described, based closely on the NEMA protocols. In the last section, the methods for a study of positron range on different tissues are described.

5.1 Scanner Geometry

5.1.1 GE Signa PET/MR

The GE Signa PET/MR system is made of five detector rings, conferring it an axial field of view (AFOV) of 25 cm. According to the hierarchy described in Section 4.1.1, the setup follows the CylindricalPET sections, as shown in Table **5.1**, including naming of components in GATE, dimensions and materials used for the model. Additionally, 12 attenuation layers are included in the geometry, modelling all the components of the scanner, including Kevlar layers, RF and copper shielding (not shown in Table **5.1**). In the end, the bore radius comes in at 60 cm. Figure **5.1** shows the modeled system via OpenGL.

Table 5.1: GE Signa PET/MR geometry hierarchy, dimensions and materials.

	Name	Dimensions $(x, y, z)^1$ [mm^3]	Material
rsector	signaModule	25.00 x 64.50 x 250.40	Air
module	signaDetUnit	25.00 x 64.50 x 47.84	Air
submodule	signaBlock	25.00 x 15.90 x 47.84	Air
crystal	signaCrystal	25.00 x 3.95 x 5.30	Air
layer	signaLYSO	25.00 x 3.95 x 5.30	LYSO

The rsector section is repeated 28 times along the 5 rings. Each submodule is composed of 36 individual LYSO crystals (4 by 9 array), providing the GE Signa with over 5,000 crystals for photon detection in a pixelated fashion. The use of pixelated detectors leads to a significant amount of dead space in the detector block due to the reflective material used to wrap each individual crystal, which prevents photon migration from one crystal to another. This dead space has also been modelled in GATE, as it will affect the performance of the scanner. The composition of the LYSO crystals used in this scanner has been provided by GE Healthcare and represent the theoretical composition and density of the crystals. In reality, there are slight fluctuations in these values, depending on the manufacturer. Details of the LYSO composition used in this model are shown in Table **5.3**.

The digitizer settings are mostly provided by GE, including energy blurring and window, time resolution, minimal sector difference and coincidence time windows. The multiples policy was set to the default *keepIfAllAreGoods* and the dead time was set at 300 ns in a non-paralyzable behavior. The specification can be seen in more detail in Table **5.5**.

---

[1] *x, y, z* according to the referential presented in Figure **5.1**.
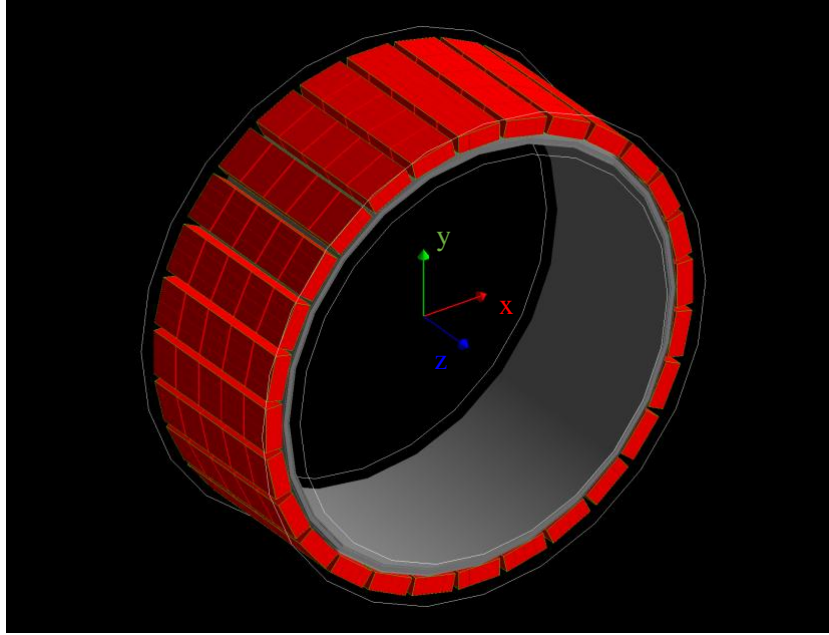
Figure 5.1: Modelled GE Signa PET/MR geometry. CylindricalPET outline in white; rsector outlined in green; detector block and crystal represented in red; 12 attenuation layers represented in gray. For scale, the axis length is 10 cm is all directions.

5.1.2 Total-Body PET

The design of the total-body PET was planned based on a fraction of the sitting height of the tallest European citizen, which is 104 cm. [77] This means this scanner would be capable of performing full torso exams on 99% of the population of Europe, without the need for translation inside the scanner. To achieve such a long AFOV, the plan includes 20 detector rings with 50 x 50 x 16 mm^3 monolithic LYSO crystals. The use of monolithic crystals reduces the dead space in the detectors, while maintaining or even increasing spatial resolution. [78] The hierarchy of the system is shown in Table **5.2** and a representation can be seen in Figure **5.2**.

Table 5.2: TB PET/MR geometry hierarchy, dimensions and materials.

	Name	**Dimensions (x, y, z)^2 [mm^3]**	**Material**
rsector	rsector	1060 x 56 x 43	Carbon Fiber
module	air_box	1040 x 52 x 40	Vacum
submodule	pcb	52 x 52 x 17	PCB
crystal	crystal	50 x 50 x 16	LYSO

The rsector is repetead 36 times along the CylindricalPET geometry, adding up to 720 monolithic crystals in the scanner. The LYSO material used in these crystals is slightly different from the one used in the GE Signa and was taken from a paper by L. Pidot et al [79]. PCB, or printed circuit board, models the electronic components that readout the crystals and process the data and has a density of 1.85 g/cm^3. The TB-PET LYSO and PCB compositions can be found in Table **5.3** and Table **5.4**, respectively. The specifications of the digitizer used for the TB-PET can be seen Table **5.5**. For consistency and due to

---

^{2} x, y, z according to the referential shown in Figure **5.2**.

uncertainty in these parameters, the multiples policy and dead time behavior were set as the same as the GE Signa.
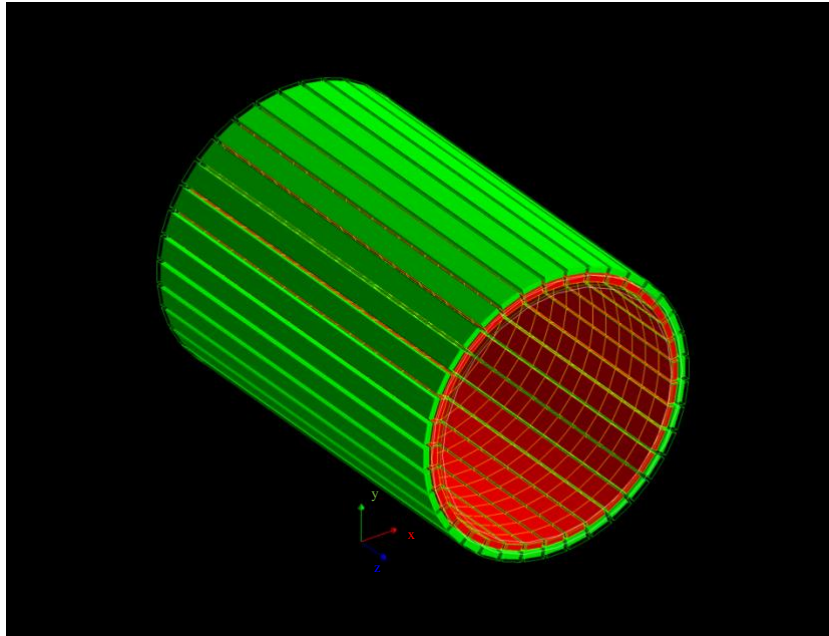
Figure 5.2: Modelled TB-PET geometry. CylindricalPET outline in white; rsector outlined in green; plastic layer represented in green; PCB outlined in yellow; monolithic crystals represented in red. For scale, the axis length is 10cm in all directions.

Table 5.3: Composition of the LYSO materials used for the GE Signa and TB-PET GATE models.

Atom	TB-PET	GE Signa
Lutetium (Lu)	0.715	0.730
Yttrium (Y)	0.040	0.028
Silicium (Si)	0.064	0.063
Oxygen (O)	0.182	0.179
Density [g/cm3]	7.11	7.21

Table 5.4: Composition of the printed circuit board used in the TB-PET geometry, which has a density of 1.85 g/cm^3.

Material	Fraction of Composition
Air	0.75
Silicon	0.20
Lead	0.05

Table 5.5: Digitizer settings for the GE Signa PET/MR and the TB-PET scanner.

Setting	GE Signa	TB-PET
Energy Blurring	12%	11.5%
Energy Window	425 - 650 keV	425 – 650 keV
Time resolution	385 ps	212.13 ps
minSectorDifference	3	5
Coincidence time window	4.9 ns	3 ns
Multiples policy	keepIfAllAreGoods	keepIfAllAreGoods
Dead time (paralyzable)	300 ns	300 ns

5.2 Sensitivity Measurements

5.2.1 Simulation Set-Up

To model the NEMA sensitivity phantom in GATE, a 700 mm long by 4 mm diameter polyethylene cylinder is created to act as the source distribution tube. This tube is placed at the center of the FOV, aligned with the axis of the scanner (z-direction). As the NEMA protocols require, 5 layers of attenuating material (aluminum) of 2.5 mm thickness each are placed sequentially around the source tube, as a way to ensure annihilation of the emitted positrons. In GATE, this means performing five different simulations, with 1 to 5 attenuation layers. The modelled and real sensitivity phantoms are represented in Figure **5.3**. The polyethylene tubes shown in the photograph are not modelled in GATE and their only purpose on the phantom is to ensure the correct placement of the tubes and the spacing between each tube.
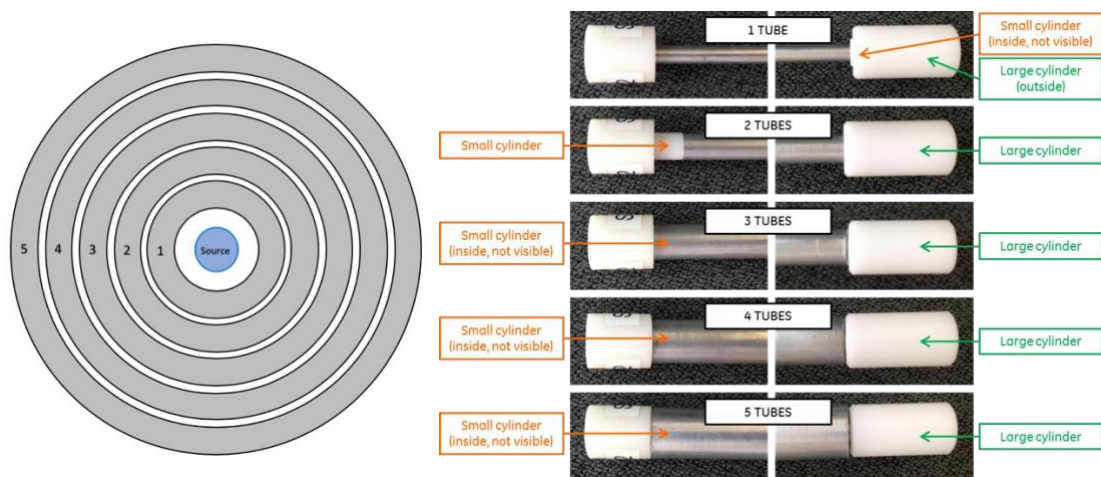
Figure 5.3: Scheme of NEMA sensitivity phantoms modelled in GATE (right); Photography of real NEMA Sensitivity phantom (left).

The activity is expected to be very low so that the count losses and random events rate are kept at less than 1% and 5%, respectively. For ^{18}F, NEMA predicts an activity of 5-10 MBq. To keep count losses and random events rate at a minimum, an activity of 5 MBq was chosen for this project, for ^{18}F. As NEMA recommends acquiring at least 10,000 coincidences and assuming that about 1% of all decays are captured by the scanner, an acquisition time of 1 second for the given activities should yield approximately 50,000 true coincidences. To account for the difference in branching ratios, the activity of radioisotopes other than ^{18}F were adjusted to yield approximately the same number of events. All used activities are presented in Table **5.6**.

Table 5.6: Activity levels of each radioisotope for NEMA Sensitivity simulations.

	^{18}F	^{11}C	^{13}N	^{15}O	^{68}Ga	^{82}Rb
Activity (MBq)	5.00	4.85	4.85	4.85	5.45	5.07

GATE's ROOT output was enabled, enabling the "Coincidences" tree and disabling all others ("*Hits*", "*Singles*") to minimize the size of the files, which can reach up to 1 GB for each layer if all trees are enabled, as opposed to up to 200 MB for just "Coincidences".

Due to the TB-PET's long AFOV, the sensitivity phantom is completely covered by the scanner bore. As an adaptation to the NEMA protocols for scanners with long AFOV, two phantoms of longer lengths were tested using ^{18}F. The used lengths were of 100 cm and 120 cm, as to have a phantom that approximated the length of the scanner, and a longer one that emits gamma photons from outside the

scanner bore, in a more realistic scenario. The allow for more accurate comparison of results, the activity concentration was maintained from the original NEMA protocol, adapting the activity to the total volume of the tube source. The data analysis is identical for all phantom sizes. For the TB-PET, this test was focused on the 100 cm long phantom for the testing of different radioisotopes.

5.2.2 Post-processing in ROOT and Excel

ROOT's "*Coincidences*" tree stores pairs of Singles that meet the conditions specified in the digitizer. Each pair is identified by an eventID for each particle (eventID1 and eventID2), which identifies the radioactive decay the Singles comes from. Furthermore, the entire history for each particle of the pair is recorded, from their original position's coordinates to the interactions (Compton or Rayleigh scattering) they suffer before reaching the detector. Here lies one of the key advantages of simulations - being able to distinguish between true, scattered or random coincidences, allowing for the measurement of 'trues only sensitivity', a situation idealized by NEMA, and the reason for performing the test with very low levels of activity.

To achieve trues only sensitivity, the situation idealized by NEMA, a C++ script ('.c' file) was developed to sort out true, random and scattered coincidences. A coincidence is considered to be random when the eventID for particle 1 differs from particle 2. When they are equal, a coincidence can still be considered scattered or true. True coincidences are obtained after checking for any Compton or Rayleigh scattering. When a true coincidence is found, its position along the z-direction (the position of where the radioactive decay took place) is stored into a 1D histogram, which can be used later to obtain an axial sensitivity distribution, or profile, for the scanner. The portion of code that sorts out the coincidence can be seen in Figure **5.4**. The complete C++ script can be found in Appendix 1. The count of each type of coincidence should also be registered.

```
if (eventID1!=eventID2) {
    nrandom++;
}
else {
    if (comptonPhantom1==0&&comptonPhantom2==0&&RayleighPhantom1==0&&RayleighPhantom2==0) {
        ntrue++;
        Sensitivity->Fill(sourcePosZ1);
    }
    else{nscatter++;
    }
}
```

Figure 5.4: Portion of the C++ script responsible for the sorting out between true, scattered and random coincidences. Complete script is found in Appendix 1.

As sensitivity is defined by NEMA as "the rate in counts per second that true coincidence events are detected for a given source strength", [67] the sensitivity for each of the attenuation layers is obtained dividing the count of true coincidences by the activity of the source. Although NEMA prescribes the correction of the count rate for the radioactive decay, taking into account the radioisotopes' half-life period and the time of the acquisition, this step was disregarded due to the short acquisition time of the simulation of only 1 second.

To obtain the system sensitivity, the data for each of the 5 layers should be made to fit the following equation:

$$S_i = S_0 \cdot \exp(-\mu_{Al} * 2 * X_i) \tag{5.1}$$

where μ_{Al} is the attenuation coefficient of the material and should be left as a variable to account for small amounts of scattered radiation, X_j is the accumulated layer thickness and S_0 is the attenuation-free

sensitivity. In this work, the fitting was done through Microsoft® Excel for Mac (Version 16.22) via exponential regression in a scatter plot, as is shown in Figure **5.5**.
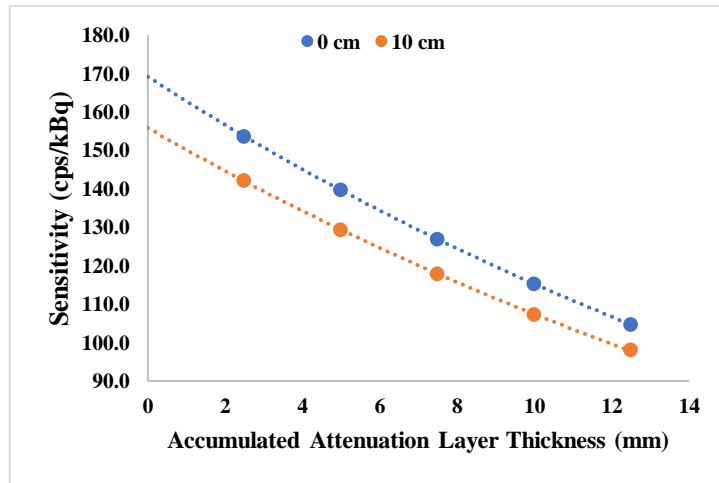
Figure 5.5: Extrapolation of the attenuation-free sensitivity value via exponential regression for simulations at the center of the FOV (blue) and with a 10 cm radial offset (orange).

This procedure is done for simulations at the center of the FOV and with a 10 cm radial offset from the center. The final reported sensitivity value is the average of both values:

$$S = \frac{S_{center} + S_{10\,cm\,off\,center}}{2} \tag{5.2}$$

5.3 Count Rate Statistics Measurements

5.3.1 Simulation Set-Up

The NEMA Standards Publications [67] prescribe the use of the NEMA Scatter phantom to perform the count rate statistics, as stated before in Section 5. In GATE, this phantom is modeled as a 700 mm long polyethylene cylinder with a diameter of 203 mm. 45 mm directly below the axial center, a 6.4 mm diameter hole is inserted, which will house the line source. The line source is modeled as a 3.2 mm diameter tube with a length equal to that of the phantom. A representation can be found in Figure **5.6**.
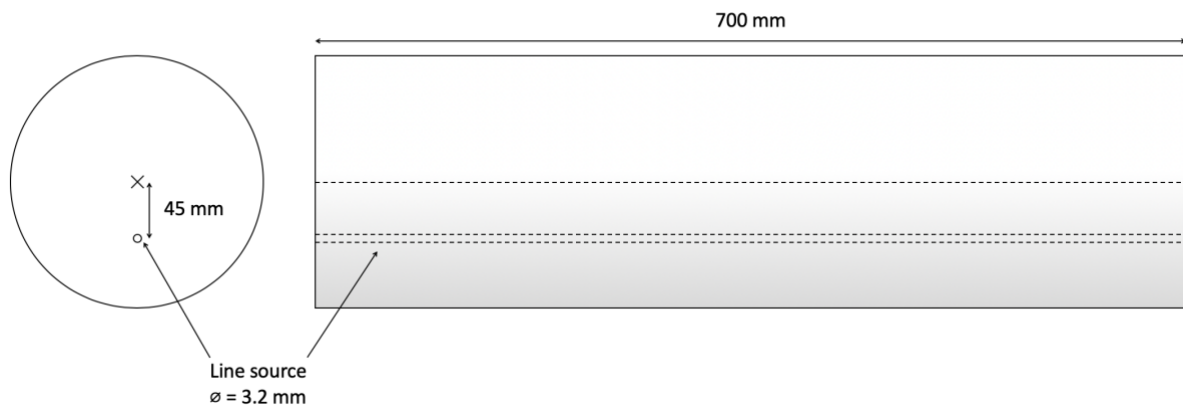
Figure 5.6: Scheme of the NEMA Scatter phantom labeled with dimensions used for its modelling in GATE.

NEMA's count rate statistics test is ran overnight in real scanners, making periodic measurements over several levels of activity in order to plot the count rates in function of the activity concentration in the line source. In GATE, to achieve such a plot, different simulations are run with different activities ranging from 1 to 900 MBq, providing the software with enough acquisition time to ensure that at least 500,000 coincidences are registered. NEMA also recommends that the activity sampling rate around the peak count rate is higher than at beginning and end of the spectrum. The acquisition time is dependent on both the scanner and the radioisotopes. The used activities in this project ranged from 1 to 900 MBq, including 10 MBq and increments of 50 MBq starting from 50 MBq onward (100 MBq, 150 MBq and so on). Although no higher sampling rate for activity is used around the peak of the count rate as is recommended by the NEMA procedures, which is expected to be at an activity close to 400 MBq for ^{18}F, this is accounted for in post processing via linear interpolation.

No scanner-intrinsic method for randoms estimation was used and the data analysis was performed by following the method described by NEMA for systems without randoms estimate.

As the TB-PET/MR has a length superior to that of the scatter phantom, in this dissertation two hypothesis to adapt the NEMA procedures to future total body scanners are proposed. First, increasing the length to 100 cm, approximating the phantom size to the AFOV width of the TB-PET studied in this thesis. Second, increasing the size to 120 cm in order to have signal originating from outside the scanner that can no longer be covered by the bore and will act as the portion of the body that is outside the scanner and take into account border effects from the edges of the AFOV. Third, two separate scatter phantoms positioned in-line on the scanner bed, composing a 'total' phantom of 140 cm. The usage of two phantoms instead of a single long one comes from the fact that the scatter phantom is quite heavy and requires assembling, which could pose multiple challenges for the user. Furthermore, with the increasing length of the phantom and the radioisotope source, it is increasingly difficult to assure the homogeneity of the source distributions, which can significantly influence results. In GATE, this last phantom includes a 3.5 cm gap between each portion due to parts of the phantom outside the polyethylene cylinder, which were not modelled on any of the hypothesis, nor on the NEMA setup described previously. However, the post-processing procedure followed is identical for all hypothesis, as described below.

5.3.2 Post-processing in ROOT and MATLAB

For this test, the analysis is based on sinograms and is aimed at estimating the rate at which the scanner acquires coincidence data, be it true, random, or scattered coincidences. Instead of recording the coincidence's position in a 1D histogram as done before, ROOT's sinogram data is extracted and written into a data file ('.dat' file) that will be later processed in MATLAB R2018a. The sinogram data consists of the angle (sinogramTheta) and the displacement (sinogramS) of the LOR, as described in more detail in Section 3.1.1. The core code of this script can be seen in Figure **5.7** and the full code can be found in Appendix 2.

```
fprintf(coincidences,"%f %f\n",sinogramTheta,sinogramS);
```

Figure 5.7: Portion of code that extracts ROOT's sinogram data. This line of code is looped over each entry in the "Coincidences" tree. The complete script can be found in Appendix 2.

The '.dat' file containing the columns of data are then read into MATLAB as a 2D matrix and transformed into a 2D histogram with 320 bins for the angle information in the vertical axis, which varies from 0 to π, and 640 bins for the displacement data in the horizontal axis, varying from -300 to 300 for the GE Signa, and -320 to 320 for the TB-PET, representing bins of 1 mm covering the entire FOV for each scanner (Figure **5.8**).
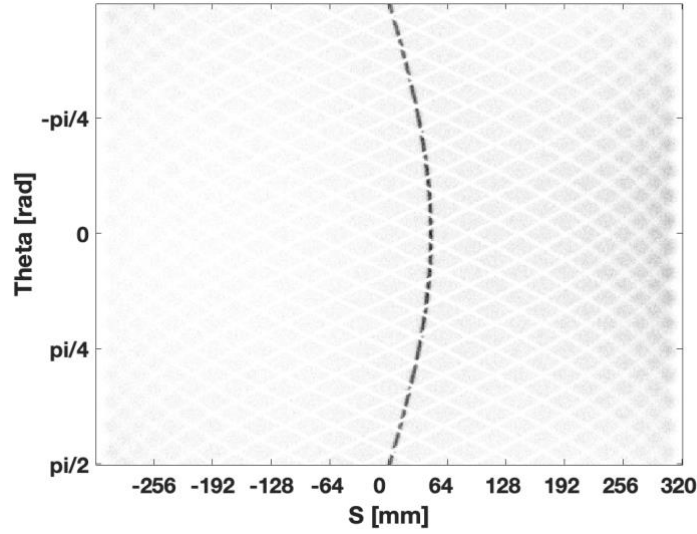
Figure 5.8: Sinogram of coincidences as extracted from ROOT. The dark line on the image represents the line source and is curved due to its positioning being 45 mm below the center of the FOV.

To make the simulation results more realistic and taking into account the limited spatial resolution of the scanner, a Gaussian blurring filter is applied to each horizontal line of the histogram (each angle). Spatial resolution is dependent on the radial offset as well as the direction of the measurement and ranges from a FWHM of 4.08 mm to 5.35 mm, for a 1 cm radial offset on the GE Signa PET/MR [80], while for the TB-PET it is 1.5 mm (FWHM). The conversion to standard deviation, σ, of the Gaussian function is found in Equations (5.4) and (5.5), according to Equation (5.3) that is used by MATLAB's *imgaussfilt3* function.

$$\text{Gaussian kernel: } f(x) = \frac{1}{\sigma\sqrt{2\pi}} e^{\frac{-(x-\mu)^2}{2\sigma^2}} \tag{5.3}$$

From this formula, the calculation of the standard deviation, σ, can be derived as:

$$\sigma = \frac{FWHM}{\sqrt{8\ln(2)}} \tag{5.4}$$

$$\sigma_{GE\ Signa} = \frac{5.35\ mm}{\sqrt{8\ln(2)}} = 2.272\ mm \xrightarrow{voxel\ edge=3.125\ mm} \sigma_{GE\ Signa} = 0.727 \tag{5.5}$$

$$\sigma_{TB-PET} = \frac{1.5\ mm}{\sqrt{8\ln(2)}} = 0.637\ mm \xrightarrow{voxel\ edge=3.125\ mm} \sigma_{TB-PET} = 0.204 \tag{5.6}$$

Following the NEMA analysis, all pixels located farther than 12cm from the center of the FOV are set to zero, as shown in Figure **5.9**.
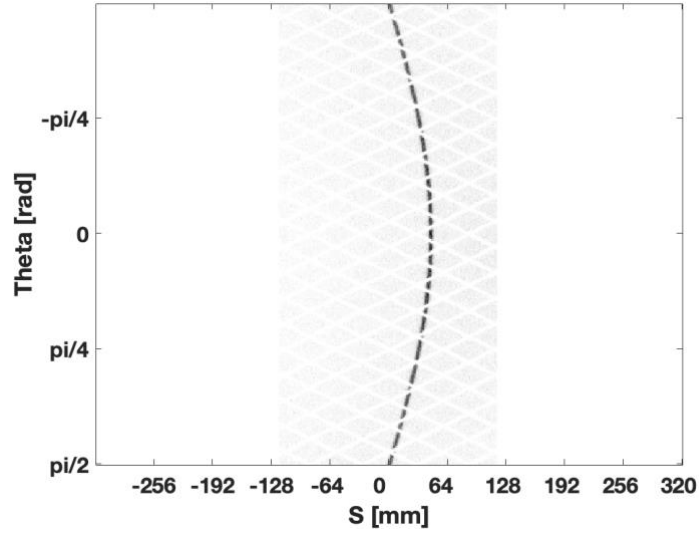
Figure 5.9: Sinogram after applying Gaussian filter and setting all pixels farther than 12 cm from the center of the FOV to zero

NEMA prescribes an alignment of the sinogram by finding the maximum value of the pixel for each projection, and shifting each angle so that the maximum value is at the center of the sinogram, with S = 0 mm, as shown in Figure **5.10**.
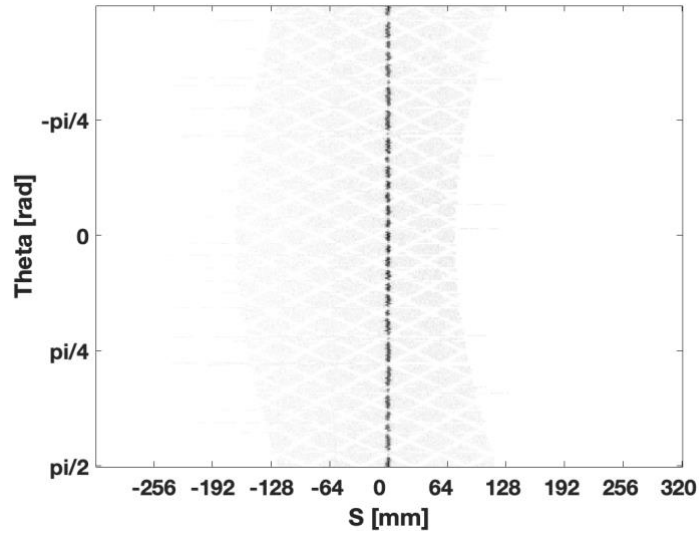
Figure 5.10: Sinogram after alignment according to the maximum values for each projection angle.

After alignment, pixels in every projection angle that have the same displacement are summed in order to obtain a sum projection, according to:

$$C(r)_{i,j} = \sum_\theta (r - S_{max}(\theta), \theta)_{i,j},$$ (5.7)

where r is the pixel, θ is the projection, and S_{max} represents the location of the pixel with the maximum value in each projection. This sum projection is shown in Figure **5.11**.

35
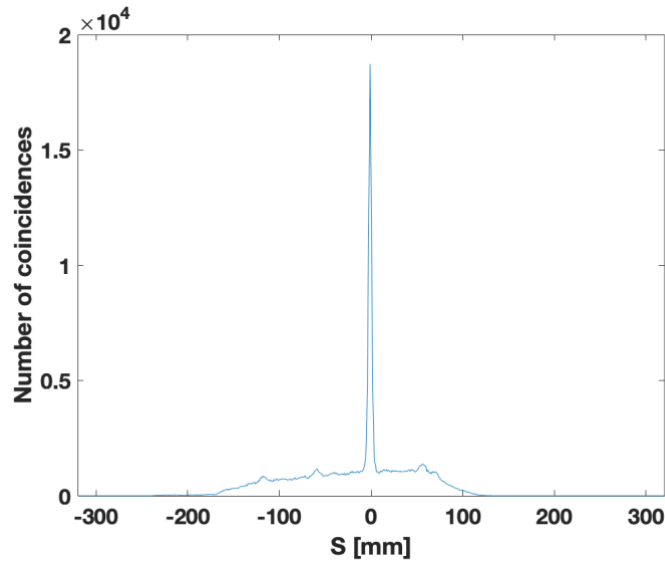
Figure 5.11: Sum projections of the sinograms. The peak on the total coincidences projection (left) originate from the line source - as expected, most coincidences come from there.

These curves are dependent on the bin size chosen for the sinograms, as wider bin sizes include more coincidences, and vice-versa. As stated before, a bin size of 1 mm was used in this work. Regardless of bin size, the integrated area under the curve remains the same and represents the total number of coincidences, C_{Total}.

In order to estimate the background counts, the NEMA procedure filters the sum projection of the total coincidences into a 40 mm wide strip (Figure **5.12**). The value of the left and right bins at the edge of the curve are then averaged and multiplied by the number of pixels in the strip. By adding this value to the number of coincidences outside the strip, the number of random plus scatter counts, C_{r+s}, is obtained. A visual representation of this procedure can be seen in Figure **5.13**.
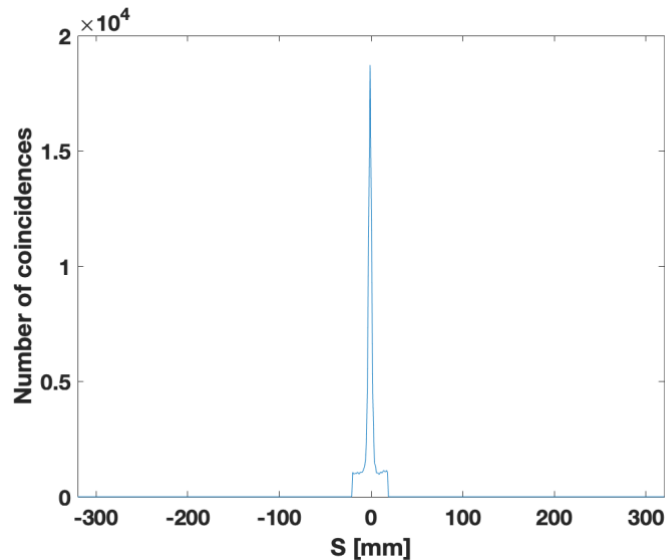
Figure 5.12: 40 mm wide strip of the total coincidence's sum projection.
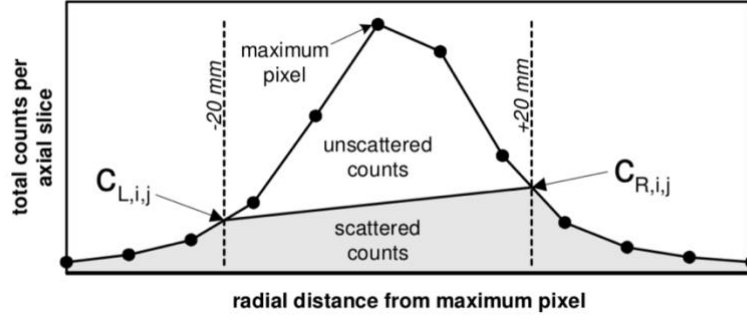
Figure 5.13: Graphical representation of NEMA procedure for calculation of background (random and scatter) counts, represented in the image in grey.

All the steps mentioned above are performed on the .m script shown in Appendix 3.

For each activity concentration A, the true, random, total and scattered events count rates are calculated by dividing the counts be the total time of acquisition:

$$R_{Total,A} = \frac{C_{Total,A}}{T_{acq,A}} \qquad (5.8)$$

$$R_{True,A} = \frac{C_{Total,A} - C_{r+s,A}}{T_{acq,A}} \qquad (5.9)$$

$$R_{Random,A} = R_{Total,A-} \left(\frac{T_{True,A}}{1 - SF} \right) \qquad (5.10)$$

$$R_{Scatter,A} = \left(\frac{SF}{1 - SF} \right) * R_{True,A} \qquad (5.11)$$

The scatter fraction is obtained only for the lowest activity acquisitions, where the count losses and randoms rate are expected to be less than 1% of the trues rate.

$$SF = \sum_{A} \frac{C_{r+s,A}}{C_{Total,A}} \qquad (5.12)$$

Having obtained all the count rates for the different types of detected coincidences, as well as the scatter fraction and NECR values for each of the simulated activity concentrations, these values can be displayed in a scatter plot against the activity concentration, allowing for a visual interpretation of the results. In addition to peak NECR, activity at peak NECR, and the scatter fraction, NEMA recommends the calculation of the NECR at specific activity concentrations as a way to investigate the integrity of the curve

For the different phantom sizes, it is important to take into account the activity concentration due to the changing source length and, consequently, volume. For the 70 cm source, this volume is of 22,000 cm^3, while for the 100 cm, 120 cm and 140 cm phantoms the volumes are of 31,000 cm^3, 38,000 cm^3 and 44,000 cm^3, respectively.

5.4 Positron Range

5.4.1 Simulation Set-Up

To estimate the positron range of different radioisotopes, the coordinates of the point where a positron is annihilated are needed, as well as the coordinates from where it originated, if possible. For this purpose, a 10 x 10 x 10 cm^3 cubic phantom with a sphere source of radius 0.1 mm placed in its center was built. No scanner geometry or digitizer was used for this part of the work. The phantom size was chosen to be large enough to ensure all positrons are annihilated within itself. The sub-millimetric radius of the source simulated a point source and allows for the simplification that every positron is originated from the origin of the referential, with coordinates $(x, y, z) = (0, 0, 0)$ cm.

The difference tissues used in phantom composition to study the effect of the magnetic field and its dependence on tissue density are specified in Table **5.7**.

Table 5.7: Phantom materials for the study of positron range.

Tissue	Density (g/cm^3)
Lung	0.26
Soft Tissue	1.00
Bone	1.42

GATE allows for particle tracking from the moment they are originated until the moment they are annihilated and prints each step of the particle's path onto the command line, or an output text file ('.txt' file), with a label. With the point source simplification, the only needed coordinates are the annihilation points, which are labeled "*annihil*" in the output. Using a Unix/Linux system, the line from the output that contains this expression can easily be printed onto a text file using command "grep" when executing the simulation, as follows:

```
Gate macroFile.mac | grep "annihil" OUTPUT.txt
```

5.4.2 Analysis

The output file originated is read onto Python 3.7.1, where the x, y and z coordinates are copied to separate variables. The three-dimensional (3D) range of each recorded positron is calculated according to Equation (5.13), looping over the individual coordinate variables.

$$R = \sqrt{x^2 + y^2 + z^2} \tag{5.13}$$

The mean 3D positron range is obtained using *numpy* function mean(). The mean positron range for each direction can only be calculated using the absolute values of the variables, otherwise the result will average at 0, and *numpy* function abs() is used before applying the mean() function. The complete '.py' script used for this analysis can be found in Appendix 4.

6 Results

The results from all the simulations regarding the sensitivity and count rate statistics tests performed on the GE Signa PET/MR and TB-PET are presented in this chapter. The results of the study on positron range are also presented.

6.1 GE Signa PET/MR

6.1.1 Sensitivity Measurements

The simulated results for the NEMA sensitivity for the GE Signa PET/MR without and with the presence of a magnetic field (0 T and 3 T, respectively) are shown in Table **6.1**. The values represent the average from simulations performed at the center of the FOV and with a 10 cm offset, according to Equation (5.2). The theoretical values were calculated based on the official GE Healthcare sensitivity for 18F, 22.5 cps/kBq, [81] and taking into account each radioisotopes' total positron branching ratio. Axial sensitivity profiles for ^{18}F and ^{82}Rb are shown in Figure **6.1** and Figure **6.2**, respectively. The coefficient of determination for the exponential regression (R^2) observed in almost all cases was close or equal to 1, indicating a strong credibility of the simulated result. The exception is ^{82}Rb, for which the regression coefficient is lower ($R^2 = 0.95$) and where the scattered points have a different distribution when compared to that of ^{18}F and all other radioisotopes, effectively influencing the regression and results (Figure **6.3**).

Table 6.1: Simulated results for the GE Signa PET/MR with and without the presence of a magnetic field. The theoretical values are based on the sensitivity value of 22.5 cps/kBq for ^{18}F, provided by GE Healthcare, [81] taking into account each radioisotope's total positron branching ratio.

Radioisotope	Positron Branching Ratio (%)	Sensitivity (cps/kBq)		
		0 T	3 T	Theoretical @ 3 T
^{18}F	96,86	20,75	21,16	22,50
^{11}C	99,75	20,53	21,07	23,21
^{13}N	99,82	20,65	21,50	23,22
^{15}O	99,89	20,31	20,95	23,24
^{68}Ga	88,88	18,10	19,06	20,68
^{82}Rb	95,45	18,78	19,87	22,20
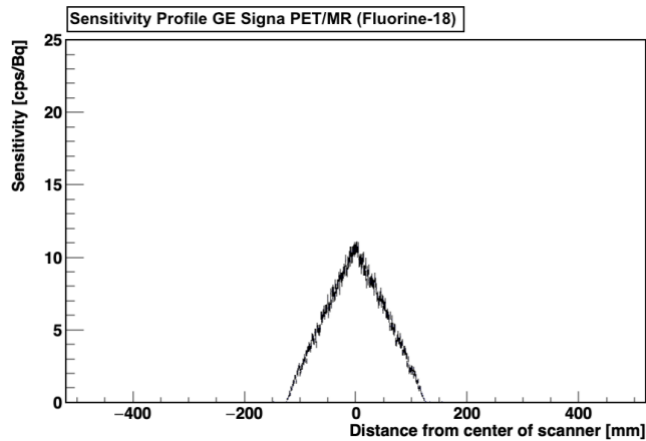
Figure 6.1: Axial sensitivity profile of the GE Signa PET/MR using ^{18}F. The histogram only extends as far as the length of the scanner.
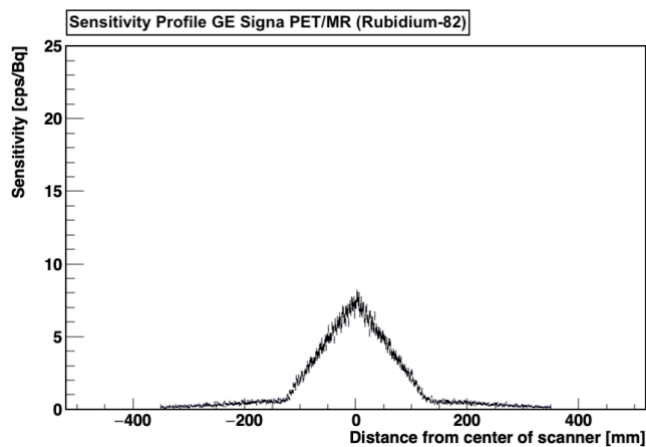
Figure 6.2: Axial sensitivity profile of the GE Signa PET/MR using ^{82}Rb. In addition to a lower peak, the histogram extends all throughout the source, with coincidences noticeably situated outside of the scanner bore.
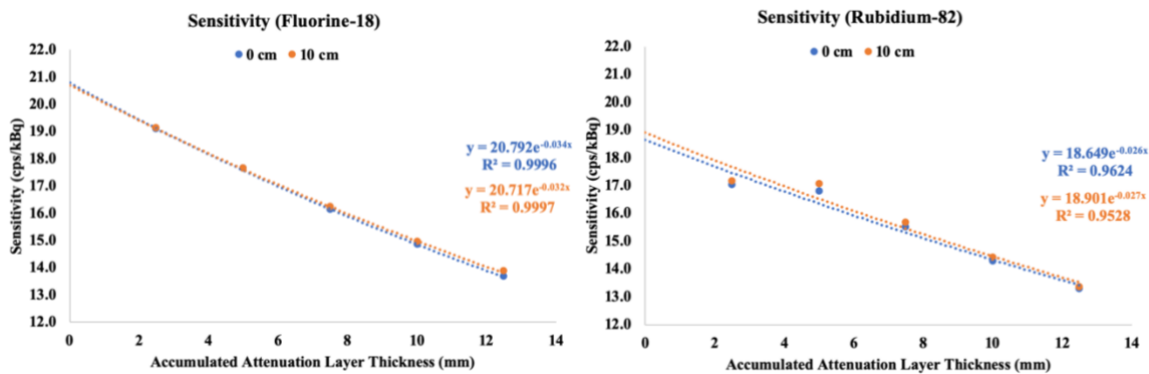
Figure 6.3: Sensitivity data plotted against the accumulated attenuation layer thickness and exponential regression of data from ^{18}F and ^{82}Rb, without the presence of a MR field. Fitted equation and coefficient of determination for both radioisotopes are presented for simulations at the center of the FOV (0 cm, blue) and for 10 cm radially off center (10 cm, orange).

6.1.2 Count Rate Statistics

On Table **6.2** the simulated NECR and related measures on the GE Signa PET/MR without a magnetic field are presented. The same measurements for the simulations with a 3 T MR field are presented in Table **6.3**. Individual rates for the true, random and scattered coincidence rates are not presented individually. The rates are dependent on the activity concentration rather than absolute activity, and so they are plotted against the activity concentration, taking into account a total volume of

22,000 ml. As recommended by NEMA, NECR obtained at activity concentration 17.5 kBq/ml and at 30.0 kBq/ml are also reported and ensure the integrity of the curves and the acceptability of the test.

Table 6.2: Results of the simulated count rate statistics test for the GE Signa PET/MR without a MR field.

Radioisotope	Peak NECR (kcps)	Activity @ peak NECR (kBq/ml)	Scatter fraction (%)	NECR @ 17.5 kBq/ml (kcps)	NECR @ 30.0 kBq/ml (kcps)
^{18}F	209,32	15,34	39,23	207,40	174,83
^{11}C	206,77	14,63	39,18	203,42	164,35
^{13}N	201,72	14,19	39,39	194,94	156,38
^{15}O	196,08	17,18	39,61	196,03	149,41
^{68}Ga	185,70	19,36	39,70	184,24	173,11
^{82}Rb	136,93	17,65	48,45	123,74	105,17

Table 6.3: Simulated results for the count rate statistics tests for the GE Signa PET/MR in the presence of a 3 T MR field.

Radioisotope	Peak NECR (kcps)	Activity @ peak NECR (kBq/ml)	Scatter fraction (%)	NECR @ 17.5 kBq/ml (kcps)	NECR @ 30.0 kBq/ml (kcps)
^{18}F	223,54	17,40	28,61	223,37	202,37
^{11}C	217,60	16,67	38,52	216,75	202,37
^{13}N	211,96	16,53	38,62	211,40	196,37
^{15}O	216,40	18,18	38,82	216,28	181,07
^{68}Ga	207,07	20,09	38,65	204,00	191,76
^{82}Rb	173,50	19,59	40,72	172,85	156,34

6.2 Total-Body PET/MR

6.2.1 Sensitivity Measurements

Table **6.4** shows the results of the sensitivity testing using ^{18}F for the TB-PET/MR with and without the presence of the 3 T magnetic field, with phantoms of different lengths but with a constant activity concentration of 0.227 kBq/ml for all lengths, which corresponds to 5 MBq, 7.14 MBq, and 8.36 MBq for the 70 cm, 100 cm, and 120 cm long phantoms, respectively. The sensitivity decreases as the length of the phantom increases but is not significantly affected by the presence of the magnetic field, for this radioisotope. The simulated sensitivity for the different tested radioisotopes using the NEMA 70 cm long phantom are shown in Table **6.5**. Under a 0 T, sensitivity is lower due to bigger positron range in the transversal plane when compared to 3 T, allowing high energy positrons to escape the phantom without being annihilated. Figure **6.4**, Figure **6.5**, and Figure **6.6** show the axial sensitivity profiles of the TB-PET sensitivity with the 70 cm, 100 cm and 120 cm long phantoms, respectively, for an ^{18}F source.

Table 6.4: Simulated sensitivity in the TB-PET to an ^{18}F source for different phantom lengths while maintaining the activity concentration in the tube source, with and without the presence of the 3 T MR field.

Phantom Length (cm)	Sensitivity (cps/kBq)	
	0 T	3 T
70	160,68	159,64
100	128,71	128,10
120	106,12	106,58
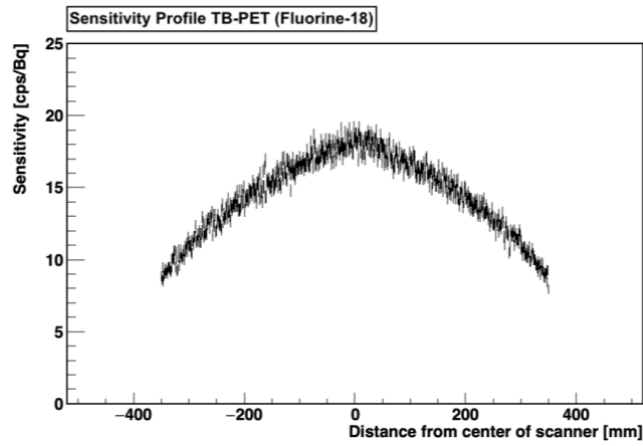
Figure 6.4: Axial sensitivity profile of the TB-PET for a 70 cm long phantom, using [18]F. As the source is completely covered by the scanner bore, coincidences are detected all throughout the source and the histogram cuts off where the source ends.
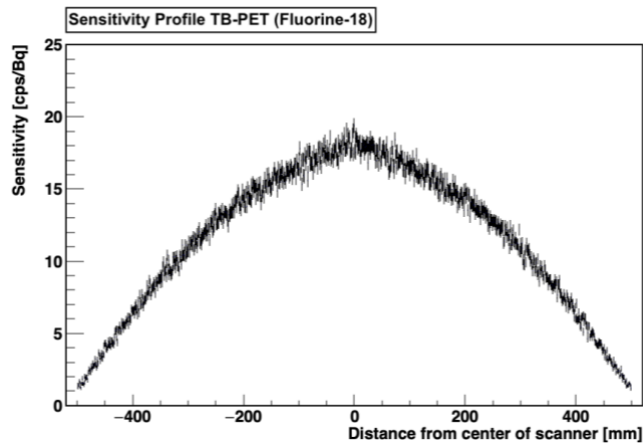
Figure 6.5: Axial sensitivity profile of the TB-PET for a 100 cm long phantom, using [18]F. As the source is completely covered by the scanner bore, coincidences are detected all throughout the source and the histogram cuts off where the source ends. The sensitivity decreases as the distance from the center of the scanner increases.
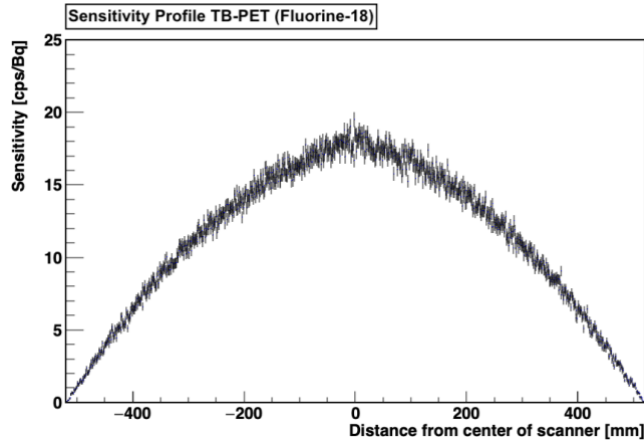
Figure 6.6: Axial sensitivity profile of the TB-PET for a 120 cm long phantom, using [18]F. Coincidences are detected all throughout the AFOV. The sensitivity decreases as the distance from the center of the scanner increases.

Table 6.5: Simulated TB-PET sensitivity for different radioisotopes with and without the presence of a 3 T MR field, using a 70 cm long phantom.

Radioisotope	Positron Branching Ratio (%)	Average Sensitivity (cps/kBq)	
		0 T	3 T
[18]F	96,86	164,58	165,70
[11]C	99,75	156,88	158,86
[13]N	99,82	174,27	177,87
[15]O	99,89	152,29	157,00
[68]Ga	88,88	135,90	147,30
[82]Rb	95,45	138,37	152,72

6.2.2 Count Rate Statistics

Table **6.7** and Table **6.7** show the simulated results of the count rate statistics test for the different phantom lengths using ^{18}F, without and with the presence of a MR field, respectively. As the rates are plotted against the activity concentration instead of absolute concentration, the total volumes used for the 70 cm, 100 cm and 120 cm to calculate concentration were of 22,000 ml, 31,000 ml and 38,000 ml, respectively. On Table **6.8** the simulated peak NECR and related measures on the TB-PET without a magnetic field are presented. The same measures for the simulations with a 3 T MR field are presented in Table **6.9**. Individual rates for the true, random and scattered coincidence rates are not presented individually. As recommended by NEMA, NECR obtained at activity concentration 17.5 kBq/ml and at 30.0 kBq/ml are also reported and ensure the integrity of the curves and the acceptability of the test.

Table 6.6: Simulated results of the count rate statistics test for TB-PET without a magnetic field (0 T), using phantoms of 70 cm, 100 cm, 120 cm, and 140 cm lengths.

Phantom Length	Peak NECR (kcps)	Activity @ peak NECR (kBq/ml)	Scatter Fraction (%)	NECR @ 17.5 kBq/ml (kcps)	NECR @ 30.0 kBq/ml (kcps)
70	1543,71	19,27	39,11	1542,45	1339,30
100	1250,14	12,95	40,19	1174,22	
120	1044,91	10,53	40,55	1044,71	-

Table 6.7: Simulated results of the count rate statistics test for TB-PET with a magnetic field (3 T), using phantoms of 70 cm, 100 cm, 120 cm, and 140 cm lengths.

Phantom Length	Peak NECR (kcps)	Activity @ peak NECR (kBq/ml)	Scatter Fraction (%)	NECR @ 17.5 kBq/ml (kcps)	NECR @ 30.0 kBq/ml (kcps)
70	1624,54	17,77	36,96	1618,52	1361,20
100	1250,14	12,95	40,19	1167,97	913,93
120	1075,47	10,53	40,14	1074,79	-

Table 6.8: Simulated results of the count rate statistics test for TB-PET without a magnetic field (0 T), using a 70 cm length phantom.

Radioisotope	Peak NECR (kcps)	Activity @ peak NECR (kBq/ml)	Scatter Fraction (%)	NECR @ 17.5 kBq/ml (kcps)	NECR @ 30.0 kBq/ml (kcps)
^{18}F	1543,71	19,27	39,11	1542,45	1339,30
^{11}C	1530,99	16,91	39,48		1338,96
^{13}N	1516,24	17,04	39,44	1516,00	1332,02
^{15}O	1501,30	16,81	39,69	1500,58	1307,34
^{68}Ga	1489,64	20,23	41,83	1480,75	1276,80
^{82}Rb	1283,25	16,81	42,73	1282,71	1154,62

Table 6.9: Simulated results of the count rate statistics test for TB-PET with a magnetic field (3 T), using a 70 cm length phantom.

Radioisotope	Peak NECR (kcps)	Activity@ peak NECR (kBq/ml)	Scatter Fraction (%)	NECR @ 17.5 kBq/ml (kcps)	NECR @ 30.0 kBq/ml (kcps)
^{18}F	1624,54	17,77	36,96	1618,52	1361,20
^{11}C	1567,18	17,04	37,28	1566,70	1383,96
^{13}N	1536,23	19,31	37,72	1532,63	1372,96
^{15}O	1516,53	20,00	38,33	1509,39	1372,35
^{68}Ga	1501,34	20,23	38,32	1492,06	1395,71
^{82}Rb	1399,59	18,18	40,32	1395,71	1239,39

6.3 Positron Range

The simulated mean 3D positron range values for different tissues with and without the presence of a 3 T MR field are shown in table Table **6.10**. It is possible to observe a reduction in positron range when going from 0 T to 3 T, an effect which is more noticeable for higher energy radioisotopes. On Table **6.11** and Table **6.12**. the transversal (x and y directions) and axial (z direction) positron ranges,

respectively, are presented. While significant changes are seen in the transversal plane, the magnetic field does not show any impact in the absolute values of the positron range in the axial direction, the same as the MR field. Annihilation point density distribution profiles are presented in Figure **6.7**, showing a spread-out density distribution in the z-direction.

Table 6.10: Mean 3D positron range in different tissues, for different radioisotopes with and without the presence of a 3 T magnetic field.

Radioisotope	Maximum Energy (keV)	Mean 3D range (mm)					
		Soft		Lung		Bone	
		0 T	3 T	0 T	3 T	0 T	3 T
^{18}F	633.5	0.50	0.49	2.23	1.70	0.34	0.34
^{11}C	960.2	1.02	0.96	3.05	1.97	0.51	0.51
^{13}N	1198.5	1.08	1.01	4.30	2.63	0.71	0.69
^{15}O	1732.0	1.87	1.66	7.74	4.28	1.22	1.17
^{68}Ga	1899.0	2.02	1.77	8.09	4.59	1.33	1.26
^{82}Rb	3378.0	4.64	3.58	18.18	9.98	3.09	2.74

Table 6.11: Mean tranversal (x or y directions) range in different tissues, for different radioisotopes with and without the presence of a 3 T magnetic field.

Radioisotope	Maximum Energy (keV)	Mean x (or y) range (mm)					
		Soft		Lung		Bone	
		0 T	3 T	0 T	3 T	0 T	3T
^{18}F	633.5	0.27	0.26	0.95	0.73	0.17	0.17
^{11}C	960.2	0.39	0.36	1.52	0.63	0.26	0.25
^{13}N	1198.5	0.54	0.49	2.15	0.74	0.35	0.34
^{15}O	1732.0	0.93	0.77	3.74	0.97	0.61	0.57
^{68}Ga	1899.0	1.01	0.82	4.04	1.00	0.66	0.61
^{82}Rb	3378.0	2.32	1.48	9.10	2.25	1.54	1.28

Table 6.12: Mean axial (z direction) range in different tissues, for different radioisotopes with and without the presence of a 3 T magnetic field.

Radioisotope	Maximum Energy (keV)	Mean z range (mm)					
		Soft		Lung		Bone	
		0 T	3 T	0 T	3 T	0 T	3T
^{18}F	633.5	0.27	0.27	0.95	1.08	0.17	0.17
^{11}C	960.2	0.39	0.39	1.52	1.5	0.26	0.26
^{13}N	1198.5	0.54	0.54	2.15	2.15	0.35	0.35
^{15}O	1732.0	0.93	0.93	3.74	3.74	0.61	0.61
^{68}Ga	1899.0	1.01	1.16	4.05	4.04	0.66	0.66
^{82}Rb	3378.0	2.32	2.32	9.09	9.08	1.55	1.55
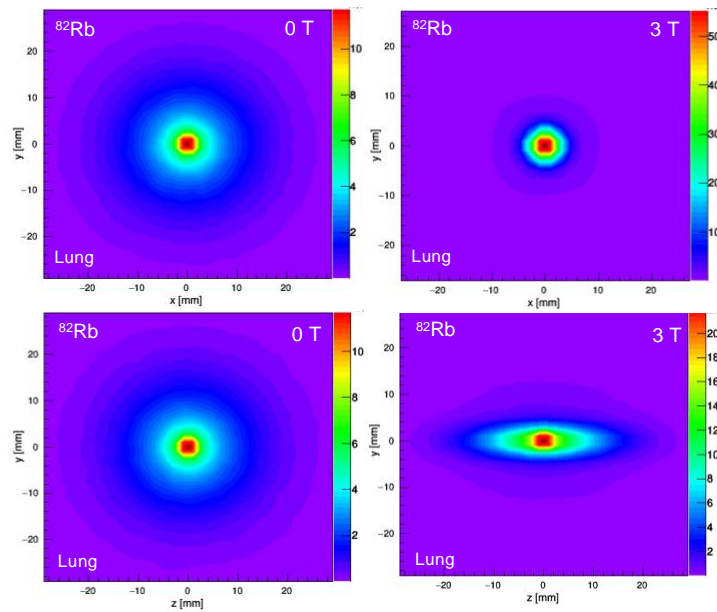
Figure 6.7: Transversal (top) and longitudinal (bottom) distributions of a point source in lung tissue with and without a 3 T magnetic field along the z direction.

7 Discussion

In this chapter, the results presented previously are discussed, as well as the limitations and drawbacks of the methods followed on this dissertation.

The results obtained for the simulated sensitivity measurement performed on GE Signa PET/MR with a 3 T MR field using a ^{18}F source, 21.16 cps/kBq, are comparable to literature values measured following the NEMA protocols, 21.5 cps/kBq [81], thus validating the simulation model. The sensitivity for the pure β^+ emitters ^{11}C, ^{13}N and ^{15}O is comparable to that of ^{18}F. The effect of the 3% extra positron emission does not significantly impact sensitivity measurements. However, ^{68}Ga and ^{82}Rb show considerable differences. For ^{68}Ga, this was to be expected as the literature values show lower sensitivity of about 2 cps/kBq less than ^{18}F [81], which is also seen in the simulations.

The case of ^{82}Rb is quite particular. With a positron branching ratio similar to ^{18}F (<2% difference), the sensitivity is much lower than what was expected. Taking a closer look at the data reveals a difference in the behavior of the radioisotope regarding the annihilation in the sensitivity phantom's attenuation layers, significantly affecting the regression method used to estimate the attenuation-sensitivity. Due to the extremely high energy of 3.381 MeV of the emitted positrons, the measurement with only one attenuation layer shows that it falls outside the trend of the rest of the measurements for this radioisotope, and the other radioisotopes. This is reflected on the coefficient of determination of the regression, which is lower than for any other tested radioisotope, significantly underestimating sensitivity for ^{82}Rb.

The sensitivity profiles for radioisotopes other than ^{82}Rb are in line with what was expected, with peak sensitivity occurring near the center of the scanner and declining towards the edge of the bore, due to geometrical and physical limitations. However, for ^{82}Rb in particular, the profile shows a significant portion of the coincidences being detected outside the scanner bore, which, in theory, should not be possible as no LOR can be placed outside the scanner when two photons are registered in the detectors. However, due to the additional 777 keV prompt-gamma emission, two gamma photons coming from the same particle can be registered inside the scanner, even when the source is outside of the scanner. Moreover, as the method for the ROOT analysis does not take into account LOR formation principles and reads only the initial positions of the detected photons, it is possible that these positions fall outside the scanner, originating the abnormal sensitivity profile we see in Figure **6.2**. This constitutes a limitation of the simulation method used in this thesis.

Without the presence of a MR field, the results across the range of radioisotopes are 1 to 5% lower than with the 3 T field present. The effect is bigger on higher energetic positrons, such as ^{82}Rb, where the coefficient of determination for the regression is also higher. This suggests an effect of the magnetic field on the positron range of the radioisotopes in the transversal plane to the direction of the magnetic field. This effect prevents the positrons from escaping the phantom tube. With the reduced range, the probability that annihilations occur in the inner layers of aluminum is higher, and the higher the sensitivity will be.

NEMA count rate statistics simulation results for ^{18}F and ^{68}Ga are in agreement with published, measured values [80], thus validating the built GATE model, as well as the analysis method. ^{11}C, ^{13}N and ^{15}O offer similar results to ^{18}F in terms of peak NECR and scatter fraction. The activity concentration

at peak NECR shows a variance that is inversely proportional to the branching ratio. For the highly energetic and non-pure emitters, ^{68}Ga and ^{82}Rb, the count rates show lower values compared to ^{18}F. These differences are attributed to the 3% and 14.16% additional gamma photons that are emitted when the radioisotopes decay to certain excited levels. These additional prompt-gammas are susceptible to Compton scattering and, in the case of ^{68}Ga, even pair production due to its high energy of 1.077 MeV, which exceeds the threshold for pair production, 1.022 MeV. Either by down-scattering onto the energy window of the detector via Compton scattering or by production of extra pairs of 511 keV photons, these additional gammas result in contamination of the acquired data, with the scanner registering more random and scattered coincidences and, in case they are considered true coincidences, most likely misplacing the LORs. Furthermore, additional prompt-gammas will be registered by the detectors and contribute to their busyness, aggravating their dead-time limitations, more significantly at high activity levels. Both these effects effectively lower the ability of the scanner to register true coincidences and lower the NECR values for both these radioisotopes. This is more prominent for ^{82}Rb, due to its prompt-gamma probability being higher and their energy being much closer to the energy window, at only 777 keV.

The move to total-body PET results in tremendous increase in both sensitivity and NECR. A 104 cm AFOV yields a sensitivity of 164.58 cps/kBq for ^{18}F, which represents a sensitivity that is almost 8 times higher than in the GE Signa, which stands at only 21.16 cps/kBq. This trend is present with all the tested radioisotopes. In what regards the count rate statistics test, the TB-PET yields a peak NECR of 1543.71 kcps for ^{18}F. In the TB-PET, the influence of the positron branching ratio as well as additional gamma photons seems to be amplified, however, the effects of the magnetic field are about the same, with an increase in sensitivity of up to 5% in the presence of the magnetic field, both in the GE Signa and the TB-PET. This suggests that the effect of the MR field is a result of the NEMA protocols and the way the tests are conducted, rather than a direct effect on performance of the scanners and may not translate directly into benefits in real patient scanning and clinical practice.

When considering longer phantoms for the sensitivity test on the TB-PET, starting to take into account border effects of the scanner, the sensitivity drops from 160.68 cps/kBq on the NEMA 70 cm phantom to 128.71 cps/kBq for the 100 cm phantom and to 106.12 cps/kBq for the 120 cm phantom, without the presence of the magnetic field. On the latter case, there is already some activity outside the scanner as the phantom is longer than the AFOV, although the activity concentration is the same all throughout the phantom. Despite being lower than the 70cm NEMA phantom, this still represents an increase of over 4 times the sensitivity of the GE Signa, and represents a more real-life simulation of the capacities of the scanner, as in patient scanning there is always some activity outside the scanner. This is also the case for the count rate statistics test, specifically peak NECR. For the 100 cm phantom, peak NECR drops to 1250.14 kcps and to 1049.91 kcps for the 120 cm phantom, still being 4 times higher than peak NECR for the GE Signa. Considering the 70 cm scanner, both measures on the TB-PET would be 7 to 8 times higher. Together, these measurements allow for the manipulation and optimization of clinical scanning protocols, regarding exam times and activity dose injected in the patient. With either faster imaging or lower dose, or a combination of both, it is possible to maintain state of the art image quality while reducing operational costs, increasing patient throughput and/or increase profit. Due to the capability of scanning with lower activities, TB-PET represents the future of PET imaging in remote areas, to where transportation times are longer.

The positron range studies confirm a strong dependency on the density of the tissue surrounding the source. The effect of the magnetic field is also clearly seen all throughout the different radioisotopes and different tissues, although it is much more prominent for high energy emitters in less dense tissues. Considering the three-dimensional mean positron range, the impact of the magnetic field is felt through a reduction of up to 50% in its value under a magnetic field, compared to no magnetic field. From a

deeper analysis, it is clear that the decrease is a result of the constraints on the range in the transversal plane to the direction of the field, which was to be expected given the physics involved, namely the Lorentz force. However, no significant changes are observed in the axial range, with all the values being unchanged when going from 0 T to 3 T. The constraints are more noticeable with the energy of the positron and can go up to 4 times smaller ranges in the x (or y) direction than in the z (axial) direction. Despite no significant changes being observed in absolute values for positron range in the z-direction, there are differences in the density distribution along this direction, showing an anisotropic profile. This strongly points out the need to re-evaluate image reconstruction algorithms for PET/MR imaging.

The simulations performed in this dissertation have a few drawbacks. For starters, the dead time digitizer settings have a certain degree of uncertainty as these values are not published by the manufacturer, in the case of the GE Signa, and, because the TB-PET is still under development, there are no certain values for the dead time yet as not all the components have been chosen or developed yet. For consistency and to allow for comparison between scanners, the same dead time was used for the GE Signa and the TB-PET. Having accurate measurements of dead time as well as its behavior (paralyzable or non-paralyzable), could introduce changes in the presented results, although the conclusion overall would be expected to remain the same. Furthermore, some literature suggests that the NEMA methods for data analysis of sensitivity via exponential regression can underestimate sensitivity when applied to simulated data. [82]

8 Conclusion

In this dissertation, a study of the performance of integrated PET/MR systems was done using a wide range of clinically available radioisotopes, covering energies from 633 keV to over 3.3 MeV. Different tests following the NEMA protocols were simulated on a realistic model of the GE Signa PET/MR, as well as on a 104 cm long state-of-the-art PET system currently under development. Also, a study of positron range and how it is affected by a static magnetic field was performed.

Significant differences in performance were found for the different tested radioisotopes, and as a result of the presence of the magnetic field. NEMA sensitivity was found to be highly dependent on the positron branching ratio, with higher ratios meaning higher sensitivity, but also suffer some underestimation for highly energetic positrons. The presence of additional prompt-gamma photons degrades a scanners ability to acquire data, due to effects of dead time and scanner busyness. The magnetic field generally improves both these measures in up to 5%. For a total-body PET scanner, NEMA performance is up to 8 times higher than a conventional, though state-of-the-art, scanner, both in terms of sensitivity and peak NECR, meaning faster and/or lower dose imaging, reduced operational costs, and possibility for new kinds of studies. Also, with the development of a new generation of scanners arises the need for adaptation of the NEMA protocols. Constraints to positron range in the transversal plane were found to be highly significant, especially in lower density tissues, when applying a magnetic field axially.

To try and overcome the limitations of the work developed in this dissertation, future projects should simulate also the NEMA spatial resolution and image quality tests, for better classification and quantification of the system's performance. However, this will only be possible when some specifications of the scanner, like dead time, are well-known. Other radioisotopes that are gaining popularity amongst the medical community can also be tested, such as ^{90}Y and ^{124}I, which were not included in this study due to lack of proper implementation in GATE and Geant4. Applying the quantified impact of the magnetic field on positron range on image reconstruction algorithms is also a necessary step on the path to better image quality and artifact elimination in PET/MR imaging. Lastly, research into the adaptation of the NEMA protocols to large AFOV PET scanners is needed, as the market is evolving in this direction and this kind of scanners, like the EXPLORER, is starting to become available.

Thesis Outcomes

Over the course of the internship at Medisip, multiple publications based, at least in part, on the work developed for this dissertation were published and presented. They are listed below, in chronological order.

- Poster MedImag1 "GE Signa Integrated PET/MR: Evaluation of Positron Range for Clinically Relevant PET Isotopes". 17th National Day on Biomedical Engineering. 30/11/2018, Brussels, Belgium.
- Abstract and oral presentation O 3 "NEMA NU 2–2007 measurements and GATE Monte Carlo simulations of GE Signa integrated PET/MR for different PET isotopes". 8th Conference on PET/MR and SPECT/MR (PSMR 2019). 15/04/2019, Munich, Germany.
- Abstract and oral presentation PHYS 02 "GE Signa Integrated PET/MR system: results of the NEMA NU2-2007 tests and a GATE Monte Carlo study of the clinically available isotopes". 19th BELNUC Symposium. 11/05/2019, Liège, Belgium.
- E-poster oral presentation EPS-106 "NEMA NU 2-2007 Measurements and GATE Monte Carlo of GE Signa integrated PET/MR for pure and non-pure positron emitters". EANM'19 – Annual Congress of the European Association of Nuclear Medicine. 14/10/2019, Barcelona, Spain.

References

[1]   P. A. M. Dirac, "A Theory of Electrons and Protons," *Proc. R. Soc. A Math. Phys. Eng. Sci.*, vol. 126, no. 801, pp. 360–365, Jan. 1930.

[2]   H. N. Wagner Jr, "A brief history of positron emission tomography (PET)," *Semin. Nucl. Med.*, vol. 28, no. 3, pp. 213–220, 1998.

[3]   M. E. Phelps, E. J. Hoffman, N. A. Mullani, and M. M. Ter-Pogossian, "Application of annihilation coincidence detection to transaxial reconstruction tomography.," *J. Nucl. Med.*, vol. 16, no. 3, pp. 210–24, Mar. 1975.

[4]   D. E. Kuhl and R. Q. Edwards, "Reorganizing Data from Transverse Section Scans of the Brain Using Digital Processing," *Radiology*, vol. 91, no. 5, pp. 975–983, Nov. 1968.

[5]   M. Reivich *et al.*, "The [18F]fluorodeoxyglucose method for the measurement of local cerebral glucose utilization in man.," *Circ. Res.*, vol. 44, no. 1, pp. 127–137, Jan. 1979.

[6]   T. Ido *et al.*, "Labeled 2-deoxy-D-glucose analogs. 18F-labeled 2-deoxy-2-fluoro-D-glucose, 2-deoxy-2-fluoro-D-mannose and 14C-2-deoxy-2-fluoro-D-glucose," *J. Label. Compd. Radiopharm.*, vol. 14, no. 2, pp. 175–183, 1978.

[7]   D. W. Townsend, "Combined Positron Emission Tomography-Computed Tomography: The Historical Perspective," *Semin. Ultrasound, CT MRI*, vol. 29, no. 4, pp. 232–235, 2008.

[8]   H. Iida, I. Kanno, S. Miura, M. Murakami, K. Takahashi, and K. Uemura, "A simulation study of a method to reduce positron annihilation spread distributions using a strong magnetic field in positron emission tomography," *IEEE Trans. Nucl. Sci.*, vol. 33, no. 1, pp. 597–600, 1986.

[9]   B. E. Hammer, N. L. Christensen, and B. G. Heil, "Use of a magnetic field to increase the spatial resolution of positron emission tomography," *Med. Phys.*, vol. 21, no. 12, pp. 1917–1920, 1994.

[10]   B. E. Hammer and N. L. Christensen, "Measurement of Positron Range in Matter in Strong Magnetic Fields," *IEEE Trans. Nucl. Sci.*, vol. 42, no. 4, pp. 1371–1376, 1995.

[11]   A. Wirrwar, H. Vosberg, H. Herzog, H. Hailing, and S. Weber, "4.5 Tesla magnetic field reduces range of high-energy positrons-potential implications for positron emission tomography," *IEEE Trans. Nucl. Sci.*, vol. 44, no. 2, pp. 184–189, 1997.

[12]   G. Soultanidis, N. Karakatsanis, G. Nikiforidis, and G. Loudos, "Study of the effect of magnetic field in positron range using GATE simulation toolkit," *J. Phys. Conf. Ser.*, vol. 317, no. 1, 2011.

[13]   R. Kraus, G. Delso, and S. I. Ziegler, "Simulation Study of Tissue-Speci fi c Positron Range Correction for the New Biograph mMR," *IEEE Trans. Nucl. Sci.*, vol. 59, no. 5, pp. 1900–1909, 2012.

[14]   N. J. Shah *et al.*, "Effects of magnetic fields of up to 9.4 T on resolution and contrast of PET images as measured with an MR-BrainPET," *PLoS One*, vol. 9, no. 4, p. e95250, 2014.

[15]   A. Kolb *et al.*, "Shine-Through in PET/MR Imaging: Effects of the Magnetic Field on Positron Range and Subsequent Image Artifacts," *J. Nucl. Med.*, vol. 56, no. 6, pp. 951–954, 2015.

[16]   S. Y. Huang, D. Savic, J. Yang, U. Shrestha, and Y. Seo, "The effect of magnetic field on positron range and spatial resolution in an integrated whole-body time-of-flight PET/MRI system," in *2014 IEEE Nuclear Science Symposium and Medical Imaging Conference*, 2014.

[17]   S. R. Cherry, R. D. Badawi, J. S. Karp, W. W. Moses, P. Price, and T. Jones, "Total-body imaging: Transforming the role of positron emission tomography," *Sci. Transl. Med.*, vol. 9, no.

381, p. eaaf6169, 2017.

[18] S. R. Cherry, T. Jones, J. S. Karp, J. Qi, W. W. Moses, and R. D. Badawi, "Total-Body PET: Maximizing Sensitivity to Create New Opportunities for Clinical Research and Patient Care," *J. Nucl. Med.*, vol. 59, no. 1, pp. 3–12, 2017.

[19] J. S. Welsh, "Beta decay in science and medicine," *Am. J. Clin. Oncol. Cancer Clin. Trials*, vol. 30, no. 4, pp. 437–439, 2007.

[20] J. Langner, "Event-Driven Motion Compensation in Positron Emission Tomography: Development of a Clinically Applicable Method," Technische Universität Dresden, 2009.

[21] S. Surti, J. S. Karp, and P. E. Kinahan, "PET instrumentation," *Radiol. Clin. North Am.*, vol. 42, no. 6, pp. 1003–1016, 2004.

[22] D. W. Townsend and M. Defrise, *Image reconstruction methods in positron tomography*, 1st ed. Geneva: CERN, 1993.

[23] M. N. Wernick and J. N. Aarsvold, *Emission Tomography: The fundamentals of PET and SPECT*, 1st ed. Oxford: Elsevier Inc., 2004.

[24] N. L. F. Bezem, "Detection of Lesions in Positron Emission Tomography," UMC Utrecht, 2017.

[25] M. Blau, W. Nagler, and M. A. Bender, "Fluorine-18: a new isotope for bone scanning.," *J. Nucl. Med.*, vol. 3, pp. 332–4, Jul. 1962.

[26] M. Blau, R. Ganatra, and M. A. Bender, "18F-fluoride for bone imaging," *Semin. Nucl. Med.*, vol. 2, no. 1, pp. 31–37, 1972.

[27] J. S. Fowler and A. P. Wolf, "Synthesis of carbon-11, fluorine-18, and nitrogen-13 labeled radiotracers for biomedical applications," Upton, NY, Jan. 1981.

[28] S. R. Banerjee and M. G. Pomper, "Clinical applications of Gallium-68," *Appl. Radiat. Isot.*, vol. 76, pp. 2–13, 2013.

[29] I. Velikyan, "68Ga-Based Radiopharmaceuticals: Production and Application Relationship," *molecules*, pp. 12913–12943, 2015.

[30] K. P. Zhernosekov *et al.*, "Processing of Generator-Produced Medical Application for," *J. Nucl. Med.*, vol. 48, pp. 1741–1748, 2007.

[31] "Tables of evaluated data and comments on evaluation," *Laboratoire National Henri Becquerel*, 2016. [Online]. Available: http://www.nucleide.org/DDEP_WG/DDEPdata.htm. [Accessed: 08-Mar-2019].

[32] T. Hara, N. Kosaka, and H. Kishi, "PET imaging of prostate cancer using carbon-11-choline.," *J. Nucl. Med.*, vol. 39, no. 6, pp. 990–995, 1998.

[33] V. Gõmez-Vallejo, V. Gaja, K. B. Gona, and J. Llop, "Nitrogen-13: Historical review and future perspectives," *J. Label. Compd. Radiopharm.*, vol. 57, no. 4, pp. 244–254, 2014.

[34] O. Muzik, R. S. Beanlands, G. D. Hutchins, T. J. Mangner, N. Nguyen, and M. Schwaiger, "Validation of nitrogen-13-ammonia tracer kinetic model for quantification of myocardial blood flow using PET," *J. Nucl. Med.*, vol. 34, no. 1, pp. 83–91, 1993.

[35] K. Yoshida, N. Mullani, and K. L. Gould, "Coronary flow and flow reserve by PET simplified for clinical applications using rubidium-82 or nitrogen-13-ammonia.," *J. Nucl. Med.*, vol. 37, no. 10, pp. 1701–12, 1996.

[36] M. Conti and L. Eriksson, "Physics of pure and non-pure positron emitters for PET: A review and a discussion," *EJNMMI Phys.*, vol. 3, no. 1, 2016.

[37] J.-F. Chatal, F. Rouzet, F. Haddad, C. Bourdeau, C. Mathieu, and D. Le Guludec, "Story of Rubidium-82 and Advantages for Myocardial Perfusion PET Imaging," *Front. Med.*, vol. 2, no. September, pp. 1–7, 2015.

[38]   J. Ducharme, A. L. Goertzen, J. Patterson, and S. Demeter, "Practical aspects of 18 F-FDG PET when receiving 18 F-FDG from a distant supplier," *J. Nucl. Med. Technol.*, vol. 37, no. 3, pp. 164–170, 2009.

[39]   "Detection Systems in PET," *Introduction to PET Physics*, 1999. [Online]. Available: https://depts.washington.edu/nucmed/IRL/pet_intro/index.html. [Accessed: 08-Apr-2019].

[40]   G. Sivulka, "Experimental Evidence for the Structure of the Atom," 2017. [Online]. Available: http://large.stanford.edu/courses/2017/ph241/sivulka2/. [Accessed: 15-Apr-2019].

[41]   M. Bernal, "Electron and Positron Interaction With Matter (Powerpoint slideshow)," 2015. [Online]. Available: https://sites.ifi.unicamp.br/mabernal/files/2015/02/CursoMC_7Eng.pdf. [Accessed: 15-Apr-2019].

[42]   F. H. Attix, *Introduction to Radiological Physics and Radiation Domisetry*. Heppenheim: John Wiley & Sons, 1986.

[43]   D. Soliman, "Augmented microscopy: Development and application of high-resolution optoacoustic and multimodal imaging techniques for label-free biological observation," Technischen Universität München, 2016.

[44]   J. H. Hubbell, "Electron-positron pair production by photons: A historical overview," *Radiat. Phys. Chem.*, vol. 75, no. 6, pp. 614–623, 2006.

[45]   T. E. of E. Britannica, "Pair production," *Encyclopaedia Britannica, inc.*, 2008. [Online]. Available: https://www.britannica.com/science/pair-production. [Accessed: 09-Apr-2019].

[46]   A. H. Compton, "A Quantum Theory of the Scattering of X-rays by Light Elements," *Phys. Rev.*, vol. 21, no. 5, pp. 483–502, May 1923.

[47]   S. R. Cherry, J. A. Sorenson, and M. E. Phelps, *Physics in Nuclear Medicine, 4th Edition*, 4th ed., vol. 105, no. 1. Philadelphia: Saunders, 2012.

[48]   "Interaction of Gamma Radiation with Matter," *Nuclear Power*, 2019. [Online]. Available: https://www.nuclear-power.net/nuclear-power/reactor-physics/interaction-radiation-matter/interaction-gamma-radiation-matter/. [Accessed: 11-Apr-2019].

[49]   D. B. Plewes and W. Kucharczyk, "Physics of MRI: A primer," *J. Magn. Reson. Imaging*, vol. 35, no. 5, pp. 1038–1054, 2012.

[50]   R. W. Brown, Y.-C. N. Cheng, E. M. Haacke, M. R. Thompson, and R. Venkatesan, *Magnetic Resonance Imaging: Physical Principles and Sequence Design*, 2nd ed. New Jersey: John Wiley & Sons, Inc, 2014.

[51]   D. W. McRobbie, E. A. Moore, M. J. Graves, and M. R. Prince, *MRI from Picture to Proton*, 3rd ed. Cambridge: Cambridge University Press, 2017.

[52]   S. Abdulah, "Slice selection," *Radiology Café*, 2019. [Online]. Available: https://www.radiologycafe.com/radiology-trainees/frcr-physics-notes/slice-selection. [Accessed: 24-Apr-2019].

[53]   D. B. Twieg, "The k -trajectory formulation of the NMR imaging process with applications in analysis and synthesis of imaging methods," *Med. Phys.*, vol. 10, no. 5, pp. 610–621, Sep. 1983.

[54]   S. Ljunggren, "A simple graphical representation of fourier-based imaging methods," *J. Magn. Reson.*, vol. 54, no. 2, pp. 338–343, Sep. 1983.

[55]   B. E. Hammer, "NMR-PET Scanner Apparatus," 4,939,464, 1990.

[56]   S. Vandenberghe and P. K. Marsden, "PET-MRI: A review of challenges and solutions in the development of integrated multimodality imaging," *Phys. Med. Biol.*, vol. 60, no. 4, pp. R115–R154, 2015.

[57]   G. Delso *et al.*, "Performance Measurements of the Siemens mMR Integrated Whole-Body PET/MR Scanner," *J. Nucl. Med.*, vol. 52, no. 12, pp. 1914–1922, 2011.

[58] C. Levin, G. Glover, T. Deller, D. McDaniel, W. Peterson, and S. H. Maramraju, "Prototype time-of-flight PET ring integrated with a 3T MRI system for simultaneous whole-body PET/MR imaging," *J. Nucl. Med.*, vol. 54, no. supplement 2, p. 148, 2013.

[59] B. J. Pichler *et al.*, "Performance Test of an LSO-APD Detector in a 7-T MRI Scanner for Simultaneous PET / MRI," *J. Nucl. Med.*, vol. 47, pp. 639–648, 2006.

[60] S. Yamamoto, K. Kuroda, and M. Senda, "Scintillator selection for MR compatible gamma detectors," in *2002 IEEE Nuclear Science Symposium Conference Record*, 2003, vol. 3, no. 5, pp. 1632–1635.

[61] J. Duffield, "How can length contraction result in electron circular motion in a magnetic field?," 2015. [Online]. Available: https://physics.stackexchange.com/q/210477. [Accessed: 08-Apr-2019].

[62] R. R. Raylman, B. E. Hammer, and N. L. Christensen, "Combined mri-pet scanner: a monte carlo evaluation of the improvements in pet resolution due to the effects of a static homogeneous magnetic field," *IEEE Trans. Nucl. Sci.*, vol. 43, no. 4 PART 2, pp. 2406–2412, 1996.

[63] D. Burdette *et al.*, "PET Artifacts from off-plane sources in high magnetic fields," *IEEE Nucl. Sci. Symp. Conf. Rec.*, pp. 3769–3774, 2008.

[64] A. A. Lammertsma, "Forward to the Past: The Case for Quantitative PET Imaging," *J. Nucl. Med.*, vol. 58, no. 7, pp. 1019–1024, 2017.

[65] N. A. Karakatsanis, M. A. Lodge, A. K. Tahari, Y. Zhou, R. L. Wahl, and A. Rahmim, "Dynamic whole-body PET parametric imaging: I. Concept, acquisition protocol optimization and clinical application," *Phys. Med. Biol.*, vol. 58, no. 20, pp. 7391–7418, 2013.

[66] K. Ho-Shon, D. Feng, R. A. Hawkins, S. Meikle, M. J. Fulham, and X. Li, "Optimized sampling and parameter estimation for quantification in whole body PET," *IEEE Trans. Biomed. Eng.*, vol. 43, no. 10, pp. 1021–1028, 1996.

[67] National Electrical Manufacturers Association, *NEMA NU 2-2007: Performance Measurements of Positron Emission Tomographs*. Rosslyn, VA, 2007.

[68] D. L. Bailey, D. W. Townsend, P. E. Valk, and M. N. Maisey, *Positron Emission Tomography: Basic Sciences*, 2nd ed. London: Springer, 2004.

[69] S. Jan *et al.*, "GATE: a simulation toolkit for PET and SPECT," *Phys. Med. Biol.*, vol. 49, no. 19, pp. 4543–4561, Oct. 2004.

[70] S. Agostinelli *et al.*, "GEANT4 - A simulation toolkit," *Nucl. Instruments Methods Phys. Res. A*, vol. 506, no. 3, pp. 250–303, 2003.

[71] J. Allison *et al.*, "Recent developments in GEANT4," *Nucl. Instruments Methods Phys. Res. A*, vol. 835, pp. 186–225, 2016.

[72] OpenGateCollaboration, "Users Guide: Defining a system." [Online]. Available: http://wiki.opengatecollaboration.org/index.php/Users_Guide:Defining_a_system. [Accessed: 01-Mar-2019].

[73] OpenGateCollaboration, "Users Guide: Materials." [Online]. Available: http://wiki.opengatecollaboration.org/index.php/Users_Guide:Materials. [Accessed: 04-Mar-2019].

[74] F. G. Knoll, *Radiation Detection and Measurement*, 3rd ed. New York: John Wiley & Sons, Inc., 2000.

[75] CERN, "About ROOT," 2014. [Online]. Available: https://root.cern.ch/about-root. [Accessed: 25-Apr-2019].

[76] OpenGateCollaboration, "Users Guide: Data Output," 2019. .

[77] A. M. Fredriks, S. Van Buuren, W. J. M. Van Heel, R. H. M. Dijkman-Neerincx, S. P. Verloove-

Vanhorick, and J. M. Wit, "Nationwide age references for sitting height, leg length, and sitting height/height ratio, and their diagnostic value for disproportionate growth disorders," *Arch. Dis. Child.*, vol. 90, no. 8, pp. 807–812, 2005.

[78] H. T. van Dam, "Monolithic scintillators and SiPMs in time-of-flight PET detectors," Technische Universiteit Delft, 2012.

[79] C. Lps *et al.*, "High Efficiency of Lutetium Silicate Scintillators ," *Pulse*, vol. 51, no. 3, pp. 1084–1087, 2004.

[80] A. M. Grant, T. W. Deller, M. M. Khalighi, S. H. Maramraju, G. Delso, and C. S. Levin, "NEMA NU 2-2012 performance studies for the SiPM-based ToF-PET component of the GE SIGNA PET/MR system," *Med. Phys.*, vol. 43, no. 5, pp. 2334–2343, Apr. 2016.

[81] P. Caribé, M. Koole, T. Deller, K. Van Laere, and S. Vandenberghe, "NEMA NU 2-2007 Performance Characteristics of GE Signa Integrated PET/MR: Impact of Using Different PET Isotopes," in *European Journal of Nuclear Medicine and Molecular Imaging*, 2017, vol. 44, no. S2, pp. 119–956.

[82] M. Khalif, S. Stute, A. Wagadarikar, and C. Comtat, "Modeling the GE Signa PET-MR with Monte-Carlo Simulations using GATE," in *2015 IEEE Nuclear Science Symposium and Medical Imaging Conference*, 2015.

Appendix

Appendix 1 – Processing of sensitivity data via ROOT (SensitivityAnalysis.c)

```
void SensitivityAnalysis()
{
    gROOT->SetStyle("Plain");
    //GateRootCoincBuffer mybuffer;

    //Lists of files to be read, histogram titles for each sensitivity
      profile, and output file to save the sensitivity profile
    char filename[5][100]={
    "OUT_1layer.root",
    "OUT_2layers.root",
    "OUT_3layers.root",
    "OUT_4layers.root",
    "OUT_5layers.root",
    };

    char histoTitle[5][200] = {
    "Sensitivity Profile GE Signa PET/MR (1 layer)",
    "Sensitivity Profile GE Signa PET/MR (2 layers)",
    "Sensitivity Profile GE Signa PET/MR (3 layers)",
    "Sensitivity Profile GE Signa PET/MR (4 layers)",
    "Sensitivity Profile GE Signa PET/MR (5 layers)",
    };

    char outFiles[5][100] = {
    "Sensitivityprofile_1layer.png",
    "Sensitivityprofile_2layers.png",
    "Sensitivityprofile_3layers.png",
    "Sensitivityprofile_4layers.png",
    "Sensitivityprofile_5layers.png",
    };


    // for cycle to loop over each file, title and output file
      for (int k=0;k<5;k++){

    TFile *f = new TFile(filename[k], "READ");

    ////// Process Hits  ///////
    TTree *htree = (TTree *) f->Get("Coincidences");
    long Hitentries = (long) htree->GetEntries(); // get number of
entries in the htree

        //   Get relevant variables to sort out coincidences
    float sourcePosZ1;
    int
comptonPhantom1,comptonPhantom2,RayleighPhantom1,RayleighPhantom2,event
ID1,eventID2;
```

```cpp
    float nrandom=0;
    float ntrue=0;
    float nscatter=0;

    TBranch *b_sourcePosZ1 = htree->GetBranch("sourcePosZ1");
    b_sourcePosZ1->SetAddress(&sourcePosZ1);

    TBranch *b_RayleighPhantom1 = htree->GetBranch("RayleighPhantom1");
    b_RayleighPhantom1->SetAddress(&RayleighPhantom1);

    TBranch *b_RayleighPhantom2 = htree->GetBranch("RayleighPhantom2");
    b_RayleighPhantom2->SetAddress(&RayleighPhantom2);

    TBranch *b_comptonPhantom1 = htree->GetBranch("comptonPhantom1");
    b_comptonPhantom1->SetAddress(&comptonPhantom1);

    TBranch *b_comptonPhantom2 = htree->GetBranch("comptonPhantom2");
    b_comptonPhantom2->SetAddress(&comptonPhantom2);

    TBranch *b_eventID1 = htree->GetBranch("eventID1");
    b_eventID1->SetAddress(&eventID1);

    TBranch *b_eventID2 = htree->GetBranch("eventID2");
    b_eventID2->SetAddress(&eventID2);

    TH1F *Sensitivity = new TH1F("Sensitivity",histoTitle[k],1040,-
520,520);

    //loop over each entry
    for (int i=0;i < Hitentries; i++)
    {
        b_sourcePosZ1->GetEntry(i);
        b_comptonPhantom1->GetEntry(i);
        b_comptonPhantom2->GetEntry(i);
        b_RayleighPhantom1->GetEntry(i);
        b_RayleighPhantom2->GetEntry(i);
        b_eventID1->GetEntry(i);
        b_eventID2->GetEntry(i);

        // sort random, true and scattered coincidences
        if (eventID1!=eventID2) {
            nrandom++;
        }
        else {
            if
(comptonPhantom1==0&&comptonPhantom2==0&&RayleighPhantom1==0&&RayleighP
hantom2==0) {
                ntrue++;
                // fill sensitivity profile (histogram)
                Sensitivity->Fill(sourcePosZ1);
            }
            else{nscatter++;
            }
        }
    }

    //The parameters LengthOfSource, simulationTime, LengthOfScanner
and Activity has to be manually adjusted
```

```
    Int_t               startingActivity=5000000;
    Double_t            simulationTime=1; //in s
    Int_t               LengthOfSource=700; // in mm
    Int_t               LengthOfScanner=250; // in mm

    // Set axis titles
    Sensitivity->GetXaxis()->SetTitle("Distance from center of scanner
[mm]");
    Sensitivity->GetYaxis()->SetTitle("Sensitivity [cps/Bq]");

     /// Normalisation factor (needed due to the use of a linesource)
    Double_t norm = (startingActivity*simulationTime)/ ((1/Sensitivity-
>GetBinWidth(100))*LengthOfSource);

    // Set histogram parameters
    Sensitivity->Scale(100*(1/norm));
    Sensitivity->SetMaximum(25);
    Sensitivity->SetMinimum(0);
    char  Profile_Name[256];
    TCanvas* P2 = new TCanvas("P2", "Sensitivity",3,28,970,632);
    P2->SetFillColor(0);
    P2->SetBorderMode(0);
    P2->cd(1);
    Sensitivity->SetMarkerColor(kBlue);
    Sensitivity->Draw();

    // Calculate Sensitivity (trues only)
    float sensitivity_truesScatters = (ntrue)/(startingActivity)*1000;
    printf("Overall sensitivity (trues+scatters): %f cps/kBq\n \n \n
\n",sensitivity_truesScatters);

     // Save sensitivity profile
    P2->SaveAs(outFiles[k]);
    }
}
```

Appendix 2 – Processing of count rate statistics test data via ROOT (NECRAnalysis.c)

```
using namespace std;

int NECRAnalysis(){

    // input .root file
    char filename[200]= {"OUTPUT_1M.root"};

    // output coincidence file
    char coincFiles[100] = {"OUTPUT/coincidences.dat"};

    // Read input .root file
    TFile *f = new TFile(filename[k], "READ");

    // create output .dat files
    FILE *coincidences;
    coincidences = fopen(coincFiles[k], "w");
    if(coincidences == NULL)
    {
      printf("Cannot open file!");
    }

    // Obtaining coincidence data
    TTree *htree = (TTree *) f->Get("Coincidences"); // Reading
Coincidences tree
    long Hitentries = (long) htree->GetEntries(); // get number of
entries in the htree

    // Get relevant variables
    float sinogramTheta,sinogramS;

    TBranch *b_sinogramTheta = htree->GetBranch("sinogramTheta");
    b_sinogramTheta->SetAddress(&sinogramTheta);

    TBranch *b_sinogramS = htree->GetBranch("sinogramS");
    b_sinogramS->SetAddress(&sinogramS);

    // loop over each entry
    for (int i=0;i < Hitentries; i++)
    {
        b_eventID1->GetEntry(i);
        b_eventID2->GetEntry(i);
        b_sinogramS->GetEntry(i);
        b_sinogramTheta->GetEntry(i);
        // print total coincidences onto coincidence.dat file into two
columns
        fprintf(coincidences,"%f %f\n",sinogramTheta,sinogramS);
    }
    //close output files
    fflush(coincidences);
    fclose(coincidences);
    }
}
```

Appendix 3 – Estimation of count rates via MATLAB (NECRSinogramAnalysis.m)

```matlab
function [C_tot,C_rs] =NECRSinogramAnalysis(inputFile)
% From the root files, the first column is the theta and the second
column
% is the distance along the LOR
coincidences=load(inputFile);
Theta=coincidences(:,1);
S=coincidences(:,2);
h_coinc=hist3([Theta,S],'Nbins',[321 641]); %2D histogram with 321 bins
for theta and 641 bins for S (1 bin = 1mm)
Coinc = length(S);


% Applying Gaussian filter to take into account the effect of limited
% spatial detection resolution
for i=1:321
  h_coinc(i,:)=imgaussfilt(h_coinc(i,:),0.652);
end

%%% NEMA ANALYSIS WITH NO RANDOMS ESTIMATE %%%
% Step 1: Remove more than 12cm from center
central_bin = (length(h_coinc)-1)/2;
hc_coinc=h_coinc; hc_coinc(:,1:(central_bin-120)) = 0;
hc_coinc(:,(central_bin+120):end)=0;

% Steps 2 and 3: Find the maximum pixel and shift rows (Alignment)
nbins=length(hc_coinc);
central_bin = round(nbins/2)-1;
for i=1:321
    maxbin = max(hc_coinc(i,:));
    [x,y] = find(hc_coinc(i,:)==maxbin);
    shift=round(central_bin-y);
    row=hc_coinc(i,:);
    row=circshift(row,[0 shift]);
    hc_coinc(i,:)=row;
end

% Step 4: Sum projection
S_coinc=sum(hc_coinc).';
C_tot=sum(S_coinc);

% Step 5: 40mm strip
Central=S_coinc((central_bin-20):(central_bin+20));

% Step 6: Average of the 2 values
B=(Central(1)+Central(41))/2*41;
C=sum(Central);
C_rs=B+(C_tot-C);


end
```

Appendix 4 – Processing of positron range data via Python (PositronRange.py)

```
***********************************************************
This code extracts the steps number, the xyz position and the positrons
ranges emitted from a source. it saves in .txt file.
Data obtained from 'tracking/verbose 1' in Gate simulation.
***********************************************************


nameOfInputFile = "OUT.txt"

saveFile = "PositronRange.txt"

##################### Data Analysis

#1 - Plotting the end-points
from mpl_toolkits.mplot3d import Axes3D
import numpy as np
import matplotlib.pyplot as plt
from matplotlib import cm
from scipy import stats
from scipy import signal

from scipy.interpolate import splrep, sproot, splev

def fwhm(x, y, k=10):
    """
    Determine full-with-half-maximum of a peaked set of points, x and
y.

    Assumes that there is only one peak present in the datasset.  The
function
    uses a spline interpolation of order k.
    """

    class MultiplePeaks(Exception): pass
    class NoPeaksFound(Exception): pass

    half_max = np.max(y)/2.0
    s = splrep(x, y - half_max)
    roots = sproot(s)

    if len(roots) > 2:
        raise MultiplePeaks("The dataset appears to have multiple
peaks, and "
                "thus the FWHM can't be determined.")
    elif len(roots) < 2:
        raise NoPeaksFound("No proper peaks were found in the data set;
likely "
                "the dataset is flat (e.g. all zeros).")
    else:
        return abs(roots[1] - roots[0])


f = np.loadtxt(nameOfInputFile)

data = f[1:1000000,1:4].copy() # X Y Z

X = data[1:1000000,0]
Y = data[1:1000000,1]
Z = data[1:1000000,2]
```

62

```python
Ax = np.abs(X)
Ay = np.abs(Y)
Az = np.abs(Z)
Alcance = np.sqrt(np.sum(data**2, axis=1)) #mm

### *********** Calculate FWHM through Histograms *************
import matplotlib.ticker as mtick


# ATENCAO Eu modifiquei Pz para Px
Px_total = data[1:1000000,0] # Y Z
Py_total = data[1:1000000,1] # Y Z
Pz_total = data[1:1000000,2] # X Y

Pz = []

for x in range(0, len(Pz_total)):
    if (abs(Pz_total[x]) < 2.5 and abs(Py_total[x]) < 2.5):
        Pz.append(Pz_total[x])

fig = plt.figure(facecolor="white")

ax = fig.add_subplot(111)

FWHM_histZ, binsZ = np.histogram(Pz,101)
SFile_Txt = np.vstack([binsZ[1:],FWHM_histZ]).T
np.savetxt(saveFile,SFile_Txt)
FWHM = fwhm(binsZ[1:], FWHM_histZ)

### *********** Print Results *************

print('==================== 0 T ====================')
print('X, Y, Z Avarage Positron Range (mm): %.2f, %.2f, %.2f' %
(Ax.mean(), Ay.mean(), Az.mean()))
print('3D Avarage Positron Range (mm): %.2f'% (Alcance.mean()))
print("FWHM Z (mm): %.2f" % (FWHM))
print("No of Anihilation: %.3g"% (data.shape[0]))

### *********** Plot Histogram *************

label = '0 T [FWHM = %.2f mm]' % (FWHM)
plt.plot(binsZ[1:], FWHM_histZ, lw=2, label=label)
plt.legend(loc='upper right')
plt.title("Positron Range (Fluorine-18)")
plt.xlabel("Z (mm)")
plt.ylabel("Number of Events")

axes = plt.gca()
axes.set_xlim([-1,1])
ax.xaxis.set_major_formatter(mtick.FormatStrFormatter('%.1f'))
ax.yaxis.set_major_formatter(mtick.FormatStrFormatter('%.0e'))

plt.show()
```